nature methods

ARTICLES

https://doi.org/10.1038/s41592-021-01208-1

Universal autofocus for quantitative volumetric microscopy of whole mouse brains

L. Silvestri[1,2,3]✉, M. C. Müllenbroich[2,3,4], I. Costantini[2,3,5], A. P. Di Giovanna[2], G. Mazzamuto[2,3], A. Franceschini[2], D. Kutra[6], A. Kreshuk[6], C. Checcucci[2,7], L. O. Toresano[7], P. Frasconi[7], L. Sacconi[2,3] and F. S. Pavone[1,2,3]

Unbiased quantitative analysis of macroscopic biological samples demands fast imaging systems capable of maintaining high resolution across large volumes. Here we introduce RAPID (rapid autofocusing via pupil-split image phase detection), a real-time autofocus method applicable in every widefield-based microscope. RAPID-enabled light-sheet microscopy reliably reconstructs intact, cleared mouse brains with subcellular resolution, and allowed us to characterize the three-dimensional (3D) spatial clustering of somatostatin-positive neurons in the whole encephalon, including densely labeled areas. Furthermore, it enabled 3D morphological analysis of microglia across the entire brain. Beyond light-sheet microscopy, we demonstrate that RAPID maintains high image quality in various settings, from in vivo fluorescence imaging to 3D tracking of fast-moving organisms. RAPID thus provides a flexible autofocus solution that is suitable for traditional automated microscopy tasks as well as for quantitative analysis of large biological specimens.

Light-sheet microscopy (LSM) is widely used for fast imaging of large, clarified specimens, such as entire mouse brains[1]. Fluorescent staining of these samples is typically achieved with whole-mount immunohistochemistry[2] (IHC), injection of viruses or tracers[3], or with transgenic strategies[4]. Despite the wide variety of labeling methods, quantitative whole-brain analysis with LSM has been achieved only using either sparse viral labeling[5] or whole-mount staining restricted to the cell body[2,6], which facilitates cell detection even at low resolution (a few microns per pixel). The quantitative application of LSM to dense staining, filling also small structures such as those present in many transgenic models and in IHC against several important proteins (for example parvalbumin), has not been reported on a brain-wide scale because of the inability to maintain subcellular resolution consistently across the entire sample. Although the microscope per se affords subcellular resolution, the presence of a macroscopic sample introduces optical aberrations, mainly defocus[7]. In low-resolution settings, the detection depth of field is large enough to tolerate even tens of microns of defocus. However, in the high-resolution LSM implementations with submicron sampling that are necessary to disentangle cell bodies in crowded environments and resolve fine neuronal processes, defocus can compromise the coincidence of the light sheet and the focal plane of the detection objective, frustrating the very principle of LSM, and introducing severe blur in the collected images.

The issue of defocus in LSM has been previously addressed using optimization methods that search for the best focus while suspending data collection and substantially reducing imaging throughput[7–10] (Supplementary Note 1). Online optimization approaches have been recently reported, but their effectiveness has been demonstrated only in samples stained against cell nuclei[11]. Autofocusing methods compatible with real-time correction are well-established in the general field of microscopy[12], however, they require reflective surfaces such as coverslips and are therefore not suitable for LSM (Supplementary Fig. 1 and Supplementary Note 2). Here we introduce RAPID, a method for real-time image-based focus stabilization that, unlike contrast optimization methods, is agnostic with respect to image content.

Results

RAPID operating principle. RAPID is based on phase detection[13], an optical principle that exploits the fact that rays passing through distinct portions of the objective pupil intersect the image plane at different lateral positions when the object is defocused (Fig. 1a). In RAPID, the two ray bundles are physically separated using a wedge plate in a conjugated Fourier plane, and the resulting images are collected with an auxiliary camera (Fig. 1b). When the focus varies, the two images are not only blurred but are also laterally displaced (Fig. 1c and Supplementary Video 1). This mutual displacement (the 'phase') is directly proportional to the focal state of the microscope (Fig. 1d and Extended Data Figs. 1–3) and thus provides a direct feedback for focus stabilization. The quantitative relation between the lateral motion of RAPID images and defocus can be obtained by considering the two ray bundles that originate from the two halves of the pupil (Supplementary Fig. 2) separately. Depending on the amount of defocus Δf, the lateral displacement of the center of mass of ray bundles (with respect to the central ray) is given by

$$\Delta x_{\pm} = \pm G \cdot \mathrm{NA} \cdot M_{\mathrm{RAPID}} \cdot \Delta f, \quad (1)$$

where $\pm$ refers to the two different halves, NA is the numerical aperture of the microscope objective used, M_{RAPID} is the effective

[1]Department of Physics and Astronomy, University of Florence, Sesto Fiorentino, Italy. [2]European Laboratory for Non-linear Spectroscopy (LENS), Sesto Fiorentino, Italy. [3]National Institute of Optics, National Research Council, Sesto Fiorentino, Italy. [4]School of Physics and Astronomy, University of Glasgow, Glasgow, UK. [5]Department of Biology, University of Florence, Sesto Fiorentino, Italy. [6]Cell Biology and Biophysics Unit, European Molecular Biology Laboratory (EMBL), Heidelberg, Germany. [7]Department of Information Engineering (DINFO), University of Florence, Sesto Fiorentino, Italy. ✉e-mail: silvestri@lens.unifi.it

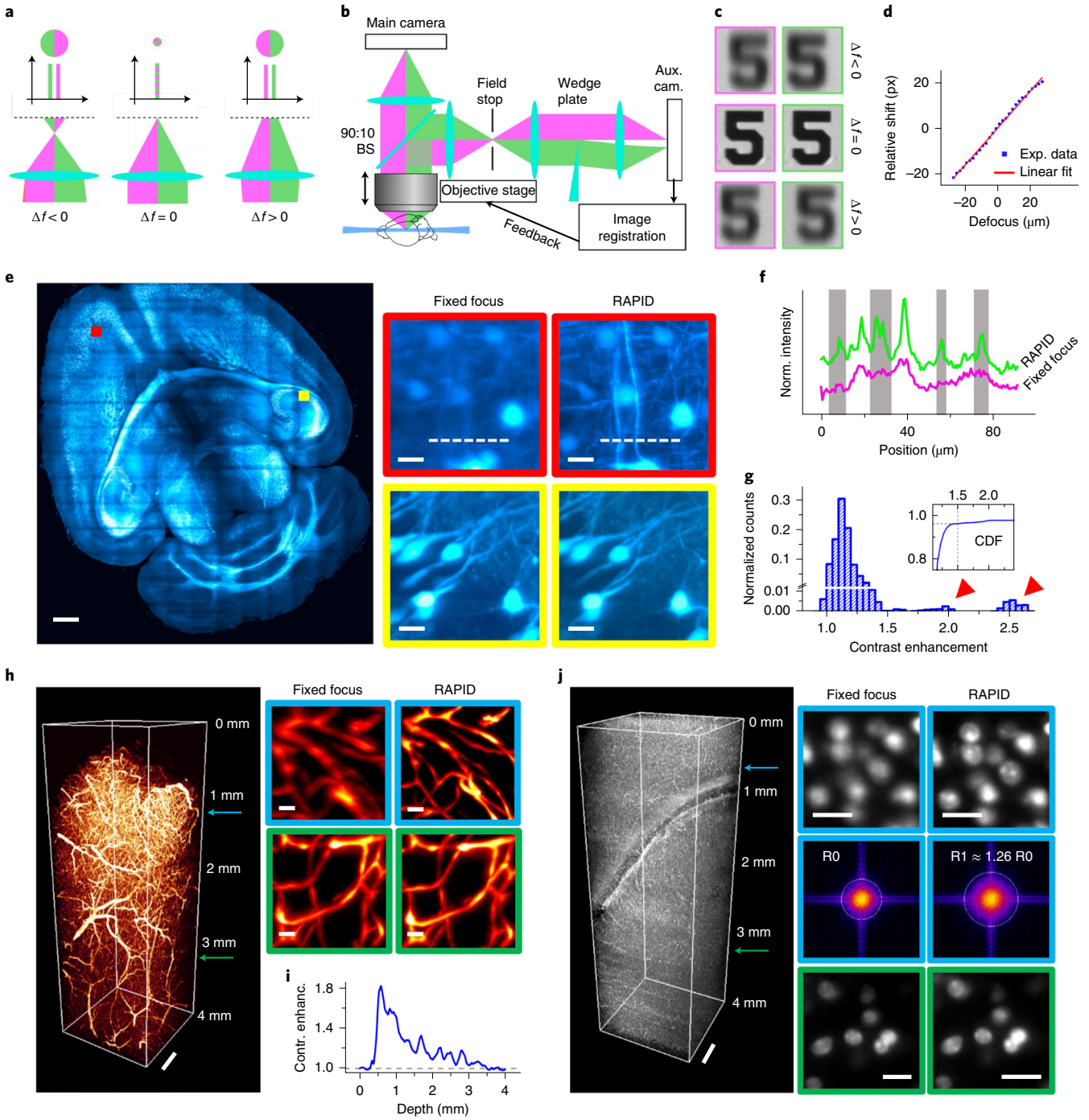

Fig. 1 | RAPID autofocusing in high-resolution LSM. a, Lateral motion of the center of mass of rays passing through different sections of the pupil, depicted in red and green. **b**, Implementation of RAPID in a standard light-sheet microscope. Aux. cam., auxiliary camera; BS, beam splitter. **c**, Lateral shift of pupil-split images. **d**, Experimental shift plotted as a function of defocus, together with a linear fit. px, pixels. **e**, A virtual slab (500 μm thick) from the brain of a thy1-GFP-M transgenic mouse, with RAPID defocus correction across different tiles (insets). Scale bar, 1 mm; insets, 20 μm. **f**, Intensity profiles along the dashed lines in the insets in **e**. Gray regions highlight the fine sample details lost without autofocus. **g**, Histogram of contrast enhancement for all the images forming the slab in **e**. Red arrowheads highlight the positive outliers, whereas the inset shows the cumulative density function (CDF). **h**, 3D rendering of an image stack from a vasculature-stained mouse brain showing insets at different depths. Scale bar, 1 mm; insets, 20 μm. **i**, RAPID contrast enhancement (contr. enhanc.) as a function of depth for the stack in **h**. **j**, 3D rendering of an image stack from a mouse brain with nuclear staining, showing insets at different depths. Scale bar, 1 mm; insets, 20 μm. The constant shape of the nuclei enables the resolution enhancement that is able to be achieved with RAPID to be evaluated using the radius of the Fourier transforms (insets, middle line).

magnification in the image space of the RAPID system, and G is a geometric factor that is dependent on the shape of the pupil portion used and on the light distribution in the pupil. In the case of two perfect halves of a uniformly filled circular pupil, G is given by $4/3\pi$ (the center of mass of half a unity circle); in general, G is of the order of unity. It follows from equation (1) that the mutual

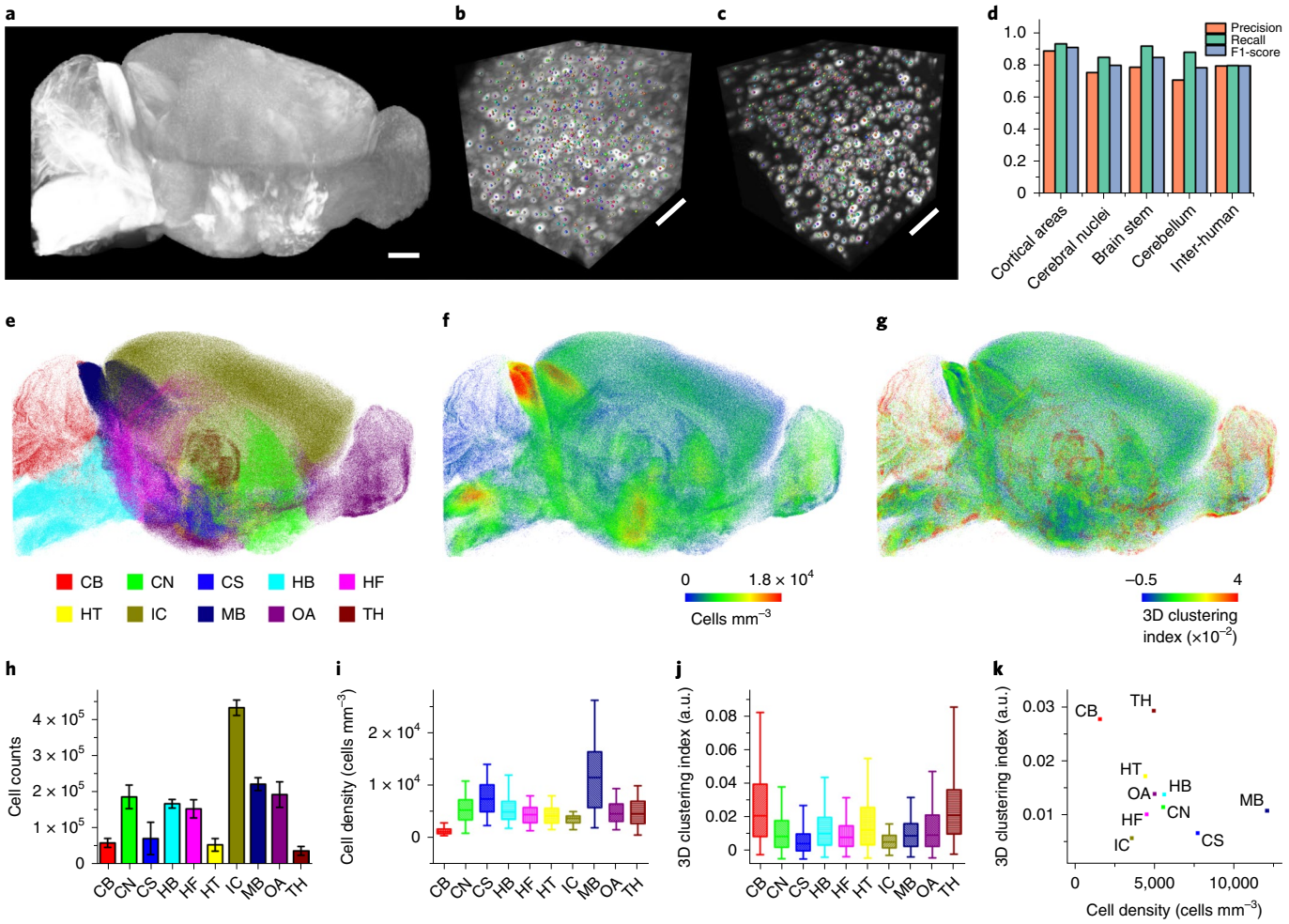

Fig. 2 | Whole-brain quantitative analysis of cell distribution. a, Sagittal maximum intensity projection of a mouse brain in which SST+ neurons express tdTomato. **b**,**c** Zoom-in renderings of the superior colliculus (**b**) and olfactory bulb (**c**). Colored dots representing the position of localized neurons are superimposed on the grayscale image. Scale bars: **a**, 1 mm; **b**,**c**, 20 µm. **d**, Performance of the cell detection algorithm in different brain areas, compared with inter-human variability in manual annotations. **e-g**, Sagittal views of the point cloud of SST+ neurons across the entire mouse brain, colored according to brain region (**e**), local cell density (**f**) or 3D clustering (**g**). CB, cerebellum; CN, cerebral nuclei; CS, cortical subplate; HB, hindbrain; HF, hippocampal formation; HT, hypothalamus; IC, isocortex; MB, midbrain; OA, olfactory areas; TH thalamus. **h**, Total cell counts in the different areas, with whiskers representing uncertainty (see Methods). **i**,**j**, Distributions of local cell density (**i**) and of 3D clustering index (**j**) (n=1,567,553 cells). a.u., arbitrary units. Data are presented as box plots with whiskers at the 5th and 95th percentiles, the central line at the 50th percentile, and the ends of the box at the 25th and 75th percentiles. **k**, Scatter plot of the average cell density versus the average 3D clustering index for different regions, highlighting important differences between the various brain areas.

distance d between the centers of mass of the two ray bundles is linearly dependent on defocus:

$$d = d_0 + a \cdot \Delta f, \tag{2}$$

with d_0 being the in-focus mutual distance and with $a = 2 \cdot G \cdot \mathrm{NA} \cdot M_{\mathrm{RAPID}}$.

The above analysis has been derived assuming a single point source. However, given that modern microscopes are usually telecentric, such analysis is valid for all the points in the field of view (and in particular G is constant throughout the field of view). Therefore, equation (2) also provides the mutual displacement of the two bidimensional images produced on the RAPID auxiliary camera. As far as the system is perfectly telecentric and spatially homogeneous (that is, neglecting vignetting and distortion), the mutual displacement between the two images is perfectly rigid (Fig. 1c and Supplementary Video 1).

Closed-loop operation of RAPID is achieved in parallel to image acquisition by inserting a beam splitter, and a motion actuator to control the detection objective (Fig. 1b). The feedback loop can be closed in a few hundreds of milliseconds, depending on the size of the auxiliary images (Supplementary Fig. 3). For sample-induced focus changes that vary more slowly than this refresh rate, RAPID effectively provides real-time focus stabilization (Supplementary Note 3). An additional guide to the choice of components for the implementation of RAPID in a given microscope can be found in Supplementary Note 4.

We experimentally verified the relation between d and Δf, and obtained d by means of cross-correlation (Supplementary Methods and Supplementary Fig. 5). Lateral shift between pupil-split images was found to be linearly dependent on defocus in a variety of illumination conditions, objective magnifications and numerical apertures (Fig. 1d and Extended Data Figs. 1–3). Exploiting this linear behavior, it is possible to infer the focal state of the system from

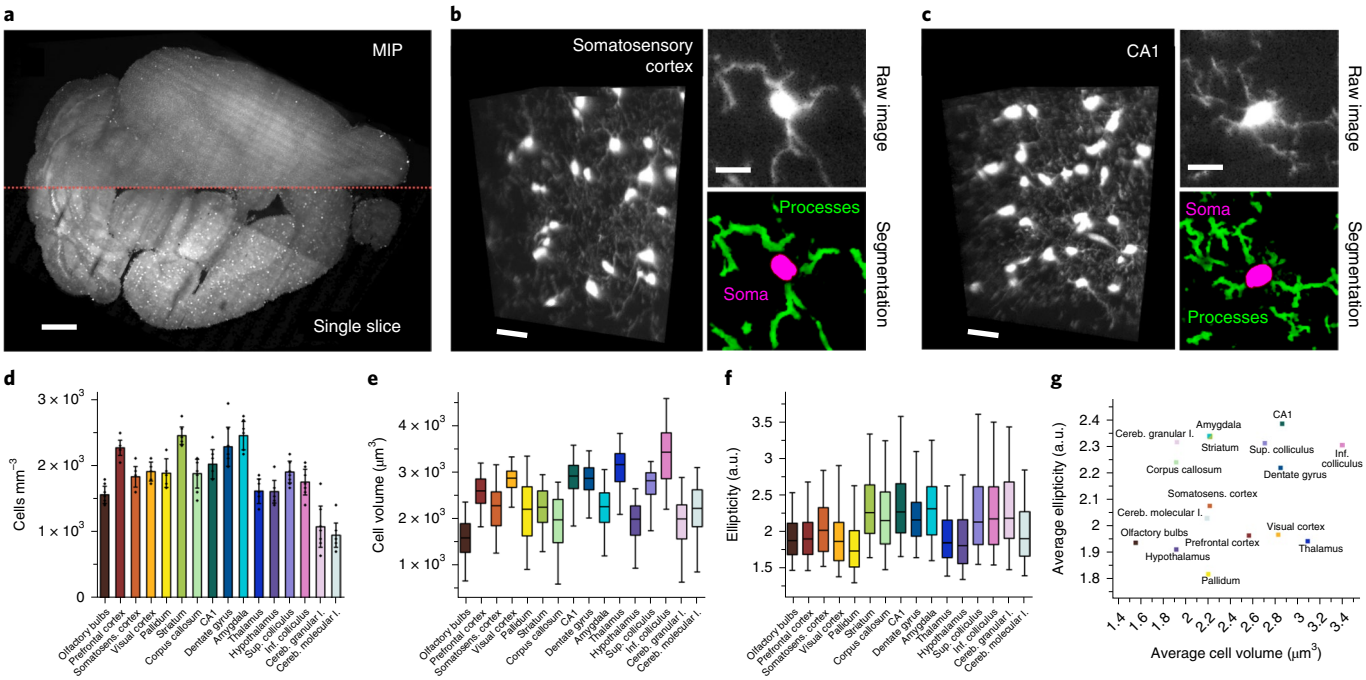

Fig. 3 | Microglia shape analysis in multiple brain areas. a, Transversal maximum intensity projection (top) and virtual slice (bottom) of a mouse brain in which the microglia cells express GFP. Scale bar, 1 mm. **b**,**c** 3D rendering of a substack extracted from the somatosensory cortex (**b**) and the CA1 (**c**) (left) and zoom-ins of a single cell (right) showing raw imaging data (top) and the results of segmentation (bottom). Scale bars: **b**,**c**, 50 μm; insets, 20 μm. **d**, Cell densities in different brain regions (mean ± s.d., $n = 8$ subvolumes; data points represent densities measured in single subvolumes). Cereb. granular l., cerebellar granular layer; cereb. molecular l., cerebellar molecular layer; inf., inferior; somatosens. cortex, somatosensory cortex; sup., superior. **e**,**f**, Distribution of cell volume (**e**) and ellipticity (**f**) (see Methods) in the same areas ($n = 3{,}685$ cells). Data are presented as box plots with the minima at the 5th percentile, the maxima at the 95th percentile, the central line at the 50th percentile, and the ends of the box at the 25th and 75th percentiles. **g**, Scatter plot of the average cell volume versus the average ellipticity for the same regions, highlighting important differences between the various brain areas.

d by inverting equation (2), and to use this information to keep the system focused using a simple feedback loop. We observed reliable focus discrimination over a range 70-fold larger than the objective depth of focus (Extended Data Fig. 3 and Supplementary Note 5). The measured focus discrimination accuracy was approximately 70% of the depth of focus (104% in the case of LSM) and can theoretically be reduced further (Supplementary Note 5 and Supplementary Table 1).

RAPID enables effective focus stabilization in LSM of cleared mouse brains. We demonstrate the capabilities of RAPID in a high-resolution light-sheet microscope designed for clarified mouse brains, and find that a feedback rate of approximately 1 Hz is sufficient to achieve proper autofocusing (Supplementary Note 3). RAPID can effectively correct defocus across different tiles (Fig. 1e and Extended Data Fig. 4), and allow the detection of small neuronal processes that are not visible without autofocus (Fig. 1f). In general, RAPID leads to a substantial increase in image contrast (18.5% ± 0.2%, 18,000 images, $P < 0.001$, Student's one-sample *t*-test), exceeding 50% in 4% of the images (Fig. 1g). Furthermore, RAPID stabilizes focus also along the stack depth and with different staining and image content, including vasculature (Fig. 1h,i and Supplementary Video 2) and nuclei (Fig. 1j). In the latter, due to the globular shape of the labeled structures, we can also quantify the resolution enhancement through the support radius of the optical transfer function[8], and we find a significant increase in resolution in out-of-focus areas (26% ± 4%, 100 images, $P < 0.001$, Student's one-sample *t*-test).

RAPID is fully compatible with a variety of clearing methods, including CLARITY (Fig. 1e), uDISCO (Extended Data Fig. 5) and PEGASOS (Extended Data Fig. 6), in line with the fact that the phase-detection principle is independent of image content or sample details. Furthermore, as long as the microscope itself is achromatic, autofocus performance is independent of the wavelength used, meaning that RAPID is also suited for multi-color imaging (Extended Data Fig. 7 and Supplementary Note 6).

RAPID-enabled LSM allows brain-wide quantitative analysis of 3D cell distribution. The superior contrast and resolution provided by RAPID enable unprecedented quantitative studies in large clarified samples. Here, we report a complete analysis of the three-dimensional (3D) spatial clustering of somatostatin-positive (SST+) neurons, a geometrical feature with profound functional implications[14,15]. As a first step, we analyzed the spatial distribution of transgenically labeled SST+ neurons across the entire mouse brain (Fig. 2a and Supplementary Video 3). The sharp, high-resolution images afforded by RAPID-enabled LSM allows reliable automatic localization of neurons (Fig. 2b,c), guaranteeing in all brain regions an accuracy that is similar or superior to the concordance between different human annotators (Fig. 2d). The same annotators failed to label neurons manually in crowded areas if the resolution was artificially lowered (Supplementary Figs. 6 and 7). Remarkably, previous LSM implementations failed to provide high-quality images amenable to automated detection of densely labeled cells across all brain regions[16]. Furthermore, localization of neurons in the absence of defocus correction fails to detect a large number of cells (Extended Data Fig. 8). In contrast, in the datasets collected with RAPID, we were able to produce a point-cloud representation of all the SST+ neurons in a mouse brain (Fig. 2e). This analysis, as well as providing counts of the SST+ neurons in each region (Fig. 2h), enabled calculation of the local 3D density of cells at the position of each single neuron, and was able to display the large

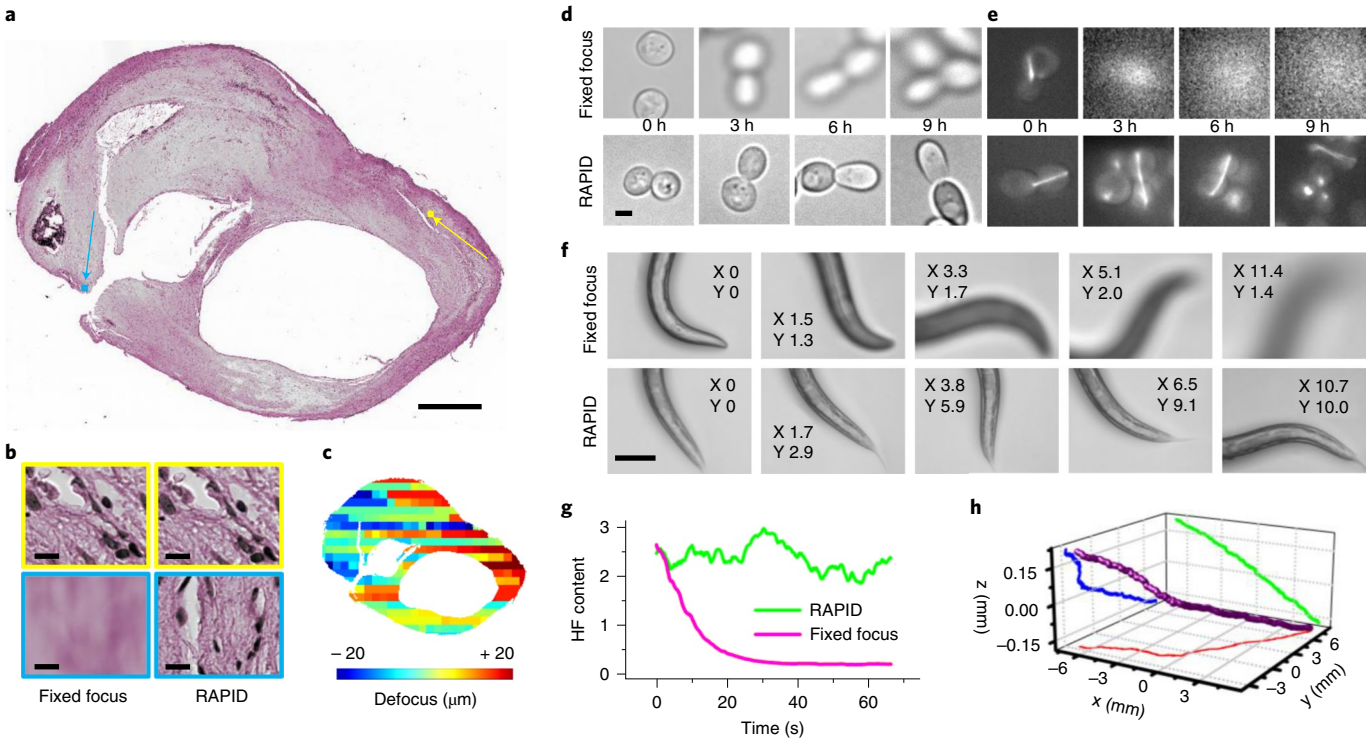

Fig. 4 | RAPID applications beyond LSM. a, The application of RAPID in whole-slide histological imaging of atherosclerotic human carotid. Scale bar, 1 mm. **b**, Insets corresponding to the yellow and blue arrows in **a**. Scale bars, 10 μm. **c**, Defocus map showing large defocus variability across the slide. **d**,**e**, Images of cultured yeast cells taken at different time points showing long-term focus stabilization with RAPID in bright-field (**d**) and epi-fluorescence (**e**) microscopy. Scale bar, 1 μm (same size images in **d** and **e**). **f**, RAPID autofocusing in imaging of fast-moving *C. elegans* nematodes; the displayed images were acquired at different *x*-*y* (planar) positions (in mm). Scale bar, 100 μm. **g**, High-frequency (HF) content of the images as a function of time. **h**, RAPID-enabled 3D tracking of the *C. elegans* worm. All experiments shown in the figure were successfully replicated on three different samples, and only a representative example per type is reported here.

variations not only between different areas but also within single regions (Fig. 2f,i and Extended Data Fig. 9). Finally, we exploited local density to estimate a clustering index based on the 3D Ripley *K*-function[17] (see Methods). This analysis shows a large variability in local 3D clustering tendency across the entire brain (Fig. 2g,j), without any apparent correlation between local density and clustering (Fig. 2k and Supplementary Fig. 8). The patchwork-like distribution of cells with a higher 3D clustering index indicates that spatial clusters of SST+ neurons are present across the whole encephalon, with large clusters clearly visible in the cerebellum and in the olfactory bulbs (Fig. 2g and Supplementary Fig. 9). Interestingly, the clustering tendency is found to be higher in deep brain areas rather than in the isocortex, suggesting potential correlations between the level of spatial clustering of SST+ interneurons and brain functions. Given that RAPID-enabled LSM enables reliable cell localization even in densely labeled samples, this kind of analysis can be scaled to other neuronal populations and developmental stages, to provide a comprehensive yet detailed view of mouse brain cytoarchitecture and complement cell counting information provided by serial sectioning methods[18].

RAPID-enabled LSM allows morphological analysis of microglia across multiple brain areas. In addition to studies on the spatial distribution of neuronal populations, the subcellular resolution enabled by RAPID allows quantitative analysis of cell morphologies on a brain-wide scale. As an example, we studied the morphology of microglia cells across the entire mouse brain (Fig. 3 and Supplementary Video 4). This is an important task in neurobiology because microglial shape is known to change according to cellular state and function[19]. Due to the whole-brain subcellular resolution afforded by RAPID-enabled LSM, we were able to segment cell bodies and processes in various brain areas (Fig. 3b,c, Extended Data Fig. 10 and Supplementary Fig. 10). Notably, the high resolution and image quality of RAPID-enabled LSM meant that this analysis could be performed using simple feature-based machine learning in ilastik, without the need for specialized deep learning pipelines and extensive manual labeling. Quantitative analysis of the shape of the soma of microglia cells highlights the different distributions of cell body volume and ellipticity in different brain areas (Fig. 3d–g). For example, we observed larger and more elliptical cells in the hippocampus than in the cortex, consistent with previous observations[20]. Together, the brain-wide morphological analysis supports the hypothesis that selected brain areas are characterized by region-specific microglia phenotypes[19].

RAPID applications beyond LSM. The real-time image-based focus stabilization of RAPID is not limited to LSM but is instead universally suited to all widefield microscopy methods and applications (Supplementary Note 7). We demonstrate RAPID operation in whole-slide histological imaging of atherosclerotic human carotid human keloid under bright-field illumination (Fig. 4a–c). The long-term stability of focus stabilization was assessed for more than 12 h by imaging living yeast cells under either bright-field or epi-fluorescence illumination (Fig. 4d,e and Supplementary Videos 7,8). Finally, high-speed defocus correction was demonstrated by imaging living *Caenorhabditis elegans* moving in 3D at speeds as high as 400 μm s^{-1} (Fig. 4f–h, Supplementary Fig. 11 and Supplementary Video 9). Notably, in this last experiment no autofocus method based on triangulation or on contrast maximization could have been used (Supplementary Note 7).

Discussion

Here we present RAPID, an image-based autofocus method that runs concurrent to data acquisition. Being agnostic to image content, this method affords robust and effective focus stabilization regardless of the labeling strategy. We exploited RAPID in LSM to image entire murine brains treated with various clearing methods, based on either tissue transformation or organic solvents, and with multiple staining methods including nuclear and vascular staining and dense labeling of neurons or microglia. Beyond LSM, we successfully applied RAPID to bright-field and epi-fluorescence microscopy. We successfully tested a wide range of numerical apertures (from 0.3 to 1.4, Supplementary Table 2), and imaging scenarios with signal-to-noise and signal-to-background ratios as low as 4.53 ± 0.07 and 1.66 ± 0.05, respectively (mean ± s.e.m., $n = 10$ images, $n = 5$ measurements per image, Supplementary Note 7). Overall, our results demonstrate the universal applicability of RAPID to the stabilization of focus in microscopy techniques based on widefield detection, the most prominent among which is LSM.

In our experiments, the RAPID refresh rate was always capable of following defocus changes in the analyzed specimens and providing effective real-time autofocusing (Supplementary Note 3). In more demanding situations, faster operation can be achieved by reducing the size of the phase comparison images or by exploiting faster devices to change focus, such as electrically tunable lenses[9] or remote refocusing with voice coil devices[21].

The pupil-split approach has the potential for fast correction of higher-order aberrations. Indeed, by dividing the pupil into more than two sectors, it would be possible to implement pupil segmentation adaptive optics[22] in a parallel rather than serial fashion, and substantially speed up wavefront detection if sufficient computational power is available to calculate cross-correlations between all the images obtained from the different pupil segments.

Given that defocus is responsible for most image degradation[23], its correction is critical; but, importantly, its correction is also sufficient to enable quantitative and comprehensive analysis of entire murine brains at subcellular resolution using LSM. RAPID unlocks the full potential of this microscopy technique, especially of novel implementations providing improved axial resolution[24], to leave the user complete choice of the labeling strategy according to experimental or financial demands. RAPID uses only off-the-shelf optical components and well-established image registration algorithms, and can be easily implemented even by non-experts in optics (Supplementary Methods). Given the simplicity of the method and its universal applicability, we anticipate that RAPID will make an important impact on the field of neuroscience and on the entire microscopy community.

Online content

Any methods, additional references, Nature Research reporting summaries, source data, extended data, supplementary information, acknowledgements, peer review information; details of author contributions and competing interests; and statements of data and code availability are available at https://doi.org/10.1038/s41592-021-01208-1.

Received: 15 July 2020; Accepted: 14 June 2021;
Published online: 26 July 2021

References

1. Ueda, H. R. et al. Whole-brain profiling of cells and circuits in mammals by tissue clearing and light-sheet microscopy. *Neuron* **106**, 369–387 (2020).
2. Renier, N. et al. Mapping of brain activity by automated volume analysis of immediate early genes. *Cell* **165**, 1789–1802 (2016).
3. Nassi, J. J., Cepko, C. L., Born, R. T. & Beier, K. T. Neuroanatomy goes viral! *Front. Neuroanat.* **9**, 44 (2015).
4. Daigle, T. L. et al. A suite of transgenic driver and reporter mouse lines with enhanced brain-cell-type targeting and functionality. *Cell* **174**, 465–480 (2018).
5. Menegas, W. et al. Dopamine neurons projecting to the posterior striatum form an anatomically distinct subclass. *eLife* **4**, e10032 (2015).
6. Murakami, T. C. et al. A three-dimensional single-cell-resolution whole-brain atlas using CUBIC-X expansion microscopy and tissue clearing. *Nat. Neurosci.* **21**, 625–637 (2018).
7. Tomer, R., Ye, L., Hsueh, B. & Deisseroth, K. Advanced CLARITY for rapid and high-resolution imaging of intact tissues. *Nat. Protoc.* **9**, 1682–1697 (2014).
8. Royer, L. A. et al. Adaptive light-sheet microscopy for long-term, high-resolution imaging in living organisms. *Nat. Biotechnol.* **34**, 1267–1278 (2016).
9. Ryan, D. P. et al. Automatic and adaptive heterogeneous refractive index compensation for light-sheet microscopy. *Nat. Commun.* **8**, 612 (2017).
10. Chen, Y. et al. A versatile tiling light sheet microscope for imaging of cleared tissues. *Cell Rep.* **33**, 108349 (2020).
11. Matsumoto, K. et al. Advanced CUBIC tissue clearing for whole-organ cell profiling. *Nat. Protoc.* **14**, 3506–3537 (2019).
12. Li, Q., Bai, L., Xue, S. & Chen, L. Autofocus system for microscope. *Opt. Eng.* **41**, 1289–1294 (2002).
13. Suda, Y., Ishizaki, A., Ohtaka, K., Akashi, A. & Hiramatsu, A. Focus detection apparatus. US patent 4,634,255 (1987).
14. Ebina, T. et al. 3D clustering of GABAergic neurons enhances inhibitory actions on excitatory neurons in the mouse visual cortex. *Cell Rep.* **9**, 1896–1907 (2014).
15. D'Souza, R. D., Bista, P., Meier, A. M., Ji, W. & Burkhalter, A. Spatial clustering of inhibition in mouse primary visual cortex. *Neuron* **104**, 588–600 (2019).
16. Ye, L. et al. Wiring and molecular features of prefrontal ensembles representing distinct experiences. *Cell* **165**, 1776–1788 (2016).
17. Ripley, B. D. The second-order analysis of stationary point processes. *J. Appl. Prob.* **13**, 255–266 (1976).
18. Kim, Y. et al. Brain-wide maps reveal stereotyped cell-type-based cortical architecture and subcortical sexual dimorphism. *Cell* **171**, 456–469 (2017).
19. de Biase, L. M. et al. Local cues establish and maintain region-specific phenotypes of basal ganglia microglia. *Neuron* **95**, 341–356 (2017).
20. Lawson, L. J., Perry, V. H., Dri, P. & Gordon, S. Heterogeneity in the distribution and morphology of microglia in the normal adult mouse brain. *Neuroscience* **39**, 151–170 (1990).
21. Weisenburger, S. et al. Volumetric Ca^{2+} imaging in the mouse brain using hybrid multiplexed sculpted light microscopy. *Cell* **177**, 1050–1066 (2019).
22. Ji, N., Milkie, D. E. & Betzig, E. Adaptive optics via pupil segmentation for high-resolution imaging in biological tissues. *Nat. Methods* **7**, 141–147 (2010).
23. Gu, M. & Sheppard, C. J. R. Effects of defocus and primary spherical aberration on images of a straight edge in confocal microscopy. *Appl. Opt.* **33**, 625 (1994).
24. Chakraborty, T. et al. Light-sheet microscopy of cleared tissues with isotropic, subcellular resolution. *Nat. Methods* **16**, 1109–1113 (2019).

Methods

RAPID implementation. In the present set-up, a 90:10 (transmission : reflection) beam splitter was placed in the infinity-corrected space behind the microscope objective in all experiments except the live imaging of fluorescent yeasts, in which a 50:50 beam splitter was used. Light reflected from the beam splitter was sent to a 4f system to create an image of the objective back aperture. The magnification of this 4f system was 200:150 for the bright-field and epi-fluorescence experiments, and 75:200 for the light-sheet experiments. In the secondary pupil plane created by the 4f system, a wedge plate (BSF2550-SIDES-A-SP, Thorlabs) was used to spatially separate the two portions of the pupil. A third lens (f = 100 mm for all experiments) was used to create two images of the microscope field of view onto an auxiliary camera, which was a Retiga SRV (QImaging) for the bright-field and epi-fluorescence experiments, and a Cascade II:512 (Photometrics) for the light-sheet experiments. A field stop was placed in the intermediate plane of the 4f system, an image plane of the microscope, to avoid superposition of the two pupil-split images. The field stop size for each experiment is given in Supplementary Table 2.

The images formed onto two pre-defined portions of the auxiliary camera were mutually aligned by determining the cross-correlation peak. Quality checks of the images and alignment, as well as several image pre-processing strategies, were used to maximize the accuracy and reliability of the system (Supplementary Methods). The mutual displacement between the pupil-split images was fed to a proportional-integrative feedback loop executed in LabVIEW 2012 (National Instruments) to correct the objective position. The RAPID software is freely available at https://github.com/lens-biophotonics/RAPID-AF. The hardware and software parameters used in the various experiments in this paper are listed in Supplementary Table 2.

Animals. For this study, we used 8–12-week-old male mice from the Jackson Laboratory. Staining of nuclei and of blood vessels was performed on C57B6J mice. The transgenic lines used were thy1-GFP-M (JAX stock no. 007788), in which a random subset of neurons express green fluorescent protein (GFP); B6N.Cg-*Sst*$^{tm2.1(cre)Zjh}$/J × B6.Cg-*Gt(ROSA)26Sor*$^{tm9(CAG\text{-}tdTomato)Hze}$/J (JAX stock nos. 018973 and 007909, respectively), in which SST+ cells express tandem dimer (td)Tomato; and B6.129(Cg)-Fos$^{tm1.1(cre/ERT2)Luo}$/J × B6.Cg-*Gt(ROSA)26Sor*$^{tm9(CAG\text{-}tdTomato)Hze}$/J (JAX stock nos. 021882 and 007909, respectively), in which neurons expressing c-fos in a given time window are labeled with tdTomato. To achieve expression of tdTomato in the last line, 50 mg kg^{-1} 4-hydroxytamoxifene dissolved in corn oil was injected at least 7 d before euthanasia, following the protocol by Guenthner et al.[25].

Brains of B6.129P2(Cg)-*Cx3cr1*^{tm1Litt}/J mice (JAX stock no. 005582), expressing GFP in microglia, were provided by F. Del Gallo from the University of Verona, Italy. All of the experimental protocols were designed in accordance with Italian laws and were approved by the Italian Ministry of Health (authorization no. 790/2016-PR). Mice were housed at 22 ± 2 °C and 55% ± 5% relative humidity, under a 12 h light–dark cycle, and were given access to food and water ad libitum.

Mouse brain clearing and staining. CLARITY[26] was used as the clearing procedure. In brief, animals were deeply anesthetized with isoflurane (1.5–2%) and then were transcardially perfused with 50 ml ice-cold 0.01 M PBS (pH 7.6), followed by 75 ml freshly prepared 4% paraformaldehyde (PFA) (w/v, pH 7.6). Brains were subsequently extracted and post-fixed in 4% PFA overnight at 4 °C. The next day, samples were incubated in a hydrogel solution (4% w/v acrylamide, 0.05% w/v bis-acrylamide and 0.25% w/v VA044 in PBS) at 4 °C for 3 d. The brains were then degassed in nitrogen atmosphere and incubated at 37 °C to initiate polymerization. The embedded samples were extracted from the gel and incubated in clearing solution (sodium borate buffer 200 mM, sodium dodecyl sulfate 4% w/v and pH 8.5) at 37 °C with gentle shaking for 1 month. Before imaging, CLARITY-treated samples were optically cleared using successive incubations in 50 ml 2,2′-thiodiethanol (30% and 63% v/v) in 0.01 M PBS (TDE/PBS)[27], each for 1 d, at 37 °C while being gently shaken.

For whole-brain nuclei staining, the CLARITY-processed murine samples were incubated at 37 °C for 2 d with a 1:50 propidium iodide (cat. no. P3566, Thermo Fisher) solution in 1X PBS–0.1% Tween 20 ($PBST_{0.1}$), followed by washing in a $PBST_{0.1}$ solution at 37 °C for 1 d. Subsequently, they were optically cleared with 63% TDE/PBS before imaging with a light-sheet microscope.

Blood vessels were stained by perfusion with a fluorescent gel as described previously[28]. Mice were euthanized by overdoses of anesthetic (isoflurane) and then transcardially perfused first with 30 ml 0.01 M PBS solution (pH 7.6) and then with 60 ml 4% w/v PFA in PBS. This was followed by perfusion with 10 ml fluorescent gel perfusate containing 0.05% tetramethylrhodamine-conjugated albumin (cat. no. A23016, Thermo Fisher) as a fluorescent marker. Mice bodies were submerged in ice water, with the heart clamped, to rapidly cool and solidify the gel. Brains were extracted after 30 min of cooling and were incubated overnight in a solution of 4% w/v PFA in PBS at 4 °C. On the next day, brains were rinsed three times with PBS. The fixed brains were incubated in a hydrogel solution for 5 d, followed by degassing and hydrogel polymerization at 37 °C. Subsequently, they were incubated in a clearing solution at 37 °C with gentle shaking for 1 month. Finally, brains were cleared in 63% TDE for imaging.

Clearing with uDISCO and PEGASOS was performed following the original protocols[29,30]. In brief, for uDISCO the PFA-fixed brains were dehydrated by incubation in a *tert*-butanol (Sigma, 360538) and water mixture at rising concentrations of 30%, 50%, 70%, 80%, 90%, 96% and 100%, for 12 h each at 35 °C. Samples were then delipidated by incubation in dichloromethane (Sigma, 270997) for 1 h, and finally cleared by incubation in a 10:1 mixture of BABB (benzyl alcohol + benzyl benzoate 1:2, Sigma, cat. nos. 24122 and W213802, respectively) and dyphenyl ether (Alfa Aesar, cat. no. A15791), with the addition of 0.4% vitamin E (Alfa Aesar, cat. no. A17039). For PEGASOS, PFA-fixed brains were decolorized in a 25% Quadrol (Sigma, cat. no. 122262) and water mixture for 2 d, then incubated in 30%, 50% and 70% *tert*-butanol–water mixtures with the addition of 3% Quadrol for 4 h, 6 h and 1 d, respectively. Samples were additionally dehydrated by a 2 d incubation in 70% *tert*-butanol, 27% PEG methacrylate Mn 500 (PEGMMA500, Sigma, cat. no. 409529) and 3% Quadrol. Finally, clearing was achieved by immersion in 75% benzyl benzoate and 25% PEGMMA500, with the addition of 3% Quadrol. All steps were performed at 37 °C.

Light-sheet microscopy. The custom-made light-sheet microscope used in the experiments has been described in detail[31]. In brief, the sample was illuminated from the side using a virtual light sheet created with a galvanometer scanner (6220H, Cambridge Technology), which was coupled via a 4f system to an air objective (Plan Fluor EPI 10X NA 0.3, Nikon) covered with a protective coverslip. Light emitted from the specimen was detected orthogonally to the illumination plane using an immersion objective corrected for clearing solutions (XLPLN10XSVMP 10X NA 0.6, Olympus). Then, it was bandpass-filtered to isolate fluorescence light and projected by a tube lens onto the chip of a scientific complementary metal-oxide-semiconductor (sCMOS) camera (Orca Flash 2.0, Hamamatsu) operating in rolling-shutter mode to guarantee confocal line detection. During imaging, the sample was fixed in a refractive index-matched quartz cuvette (cat. no. 3/Q/15/TW, Starna Scientific) and moved using a set of high-accuracy linear translators (cat. no. M-122.2DD, Physik Instrumente). Defocus correction was implemented by moving the objective with an additional identical linear translation stage. The entire system was controlled by custom software written in LabVIEW 2012 using the Murmex library (Distrio). The software can be freely downloaded at https://github.com/ludovicosilvestri/RAPID_CLSM.

Image analysis. Tiles from whole-slide imaging were stitched together using the FIJI Grid/Collection stitching plugin[32] (https://fiji.sc). FIJI was also used to produce the images and videos. The 3D rendering was performed with Amira 5.0 (FEI Visualization Sciences Group). The high-frequency content of the nematode time-lapse images was evaluated using a MATLAB R2016 script (MathWorks). Tiled images acquired with LSM were stitched together using ZetaStitcher (https://github.com/lens-biophotonics/ZetaStitcher). As well as generating a low-resolution view of the entire imaging volume, this software includes an application programming interface (VirtualFusedVolume) to access the high-resolution volume. The image contrast of the original images was evaluated using the discrete cosine transform entropy method[8] and was implemented using MATLAB R2016. Image resolution increase was evaluated by calculating the support radius in Fourier space of the optical transfer function (OTF)[8]. To calculate the support radius, the radial average of the OTF was calculated for each image, and the support radius was defined as the radius for which this average dropped below a threshold, defined as 1 log unit above the minimum plateau.

Whole-brain cell detection. Fluorescence-labeled neurons were localized in the whole-brain images using a modified version of BrainCell Finder[33]. In brief, patches of the original dataset (accessed via VirtualFusedVolume) were fed into a UNet with four contraction layers of 3D convolutions with an exponentially increasing number of filters, and four expansion layers of transposed 3D convolutions with a decreasing number of filters. UNet training was carried out with binary cross-entropy loss and Adam optimizer. The goal of this network is to perform semantic deconvolution, that is, to transform the original image into an ideal one in which cell bodies are clearly visible, while other structures such as dendrites and axons are removed. The network was previously trained on a ground-truth dataset in which a human expert has localized the centers of neuronal somata. The training dataset was composed of 162 image stacks for a total volume of approximately 5 mm^3 and 15,355 manually labeled cells. The stacks were randomly selected from different areas of the brain, to train the network to recognize the large variability in cell shape that can be found across the sample. The images deconvolved by the network are then processed with a standard blob detection algorithm (difference of Gaussians, DoG) to identify the center of bright structures, which in this case are the neurons. The overall performance of the method is evaluated by comparing the list of neuron centers found by the software with the human-annotated ground-truth test set of 165 image stacks for a total volume of approximately 5.1 mm^3 and 12,909 manually labeled cells. Again, these stacks were randomly selected from different areas of the brain, to test network performance in different brain regions. If two neuron centers from the two annotations (automatic and manual) are closer than 10 µm (approximately half of the average diameter of a neuron), they are considered to be the same cell,

that is, a true positive (TP). If a center is present only in the manual annotation, it is considered a false negative (FN), whereas if it is present only in the results of the algorithm, it is considered a false positive (FP). The counting of true positives, false positives and false negatives was carried out using the maximum bipartite matching algorithm[34]. We evaluated localization performance using the formulas precision = TP/(TP + FP) and recall = TP/(TP + FN), and the F1-score, which is defined as the harmonic mean of precision and recall. For our test set, the precision was 0.83, the recall was 0.90 and the F1-score was 0.86.

Spatial registration to atlas. A downsampled version of the whole-brain dataset (voxel size, 25 µm) was spatially registered to the Allen reference atlas using Advanced Normalization Tools[35], with a sequence of rigid, affine and diffeomorphic (that is, symmetric normalization) transformations. The same transformations were applied to the point cloud produced by the BrainCell Finder, to represent the position of SST+ neurons. Each cell was then assigned to a selected brain area based on its position. To evaluate errors in cell counting introduced by misalignment with the atlas, for each brain region we counted the number of cells lying on the region border, weighted with a 3D Gaussian kernel with a sigma of 75 µm.

Whole-brain spatial clustering analysis. To assess the spatial clustering of neurons, for each neuron we evaluated the 3D Ripley *K*-function[17]. Given the spatial density of cells λ, the *K*-function is defined as:

$$K(r) = \frac{\text{number of cells in a ball of radius r}}{\lambda}.$$

In three dimensions, under the hypothesis of complete spatial randomness (CSR), the expected value of $K(r)$ is simply the volume of the sphere:

$$E\left[K(r)\right]_{\text{CSR}} = \frac{4\pi r^3}{3}.$$

As discussed by Jafari-Mamaghani et al.[36], deviations from the CSR hypothesis are best described as the deviations from this expected value, that is, $K(r) - E[K(r)]_{\text{CSR}}$. We define the 3D clustering index, I, as the defined integral of this function on a specific range of r:

$$I = \int_{r_{\min}}^{r_{\max}} K(r) - E\left[K(r)\right]_{\text{CSR}}\, dr.$$

We chose this definition given the linear nature of the integration operator.

To estimate the *K*-function from our point cloud, we first evaluated for each neuron the local density of cells in a ball of radius 300 µm surrounding the neuron itself. This sphere is substantially larger than cell size but is still smaller than the main anatomical subdivision of the mouse brain. After estimating the local density at the position of each single neuron, we computed the 3D clustering index using the above formula, with $r_{\min} = 10$ µm (similar to cell size) and $r_{\max} = 100$ µm (smaller than the radius used for density estimation), with an integration step of 10 µm. The local density as well as the 3D clustering index were associated with each cell and were used for subsequent analysis. Images of the point clouds were produced using CloudCompare (https://www.cloudcompare.org). Graphs of the distribution of densities and of 3D clustering index were produced using OriginLab (https://www.originlab.com).

Microglia morphological analysis. Substacks from selected brain regions were manually extracted from the whole-brain dataset. Microglia somata were segmented using ilastik[37]. In more detail, we used the Autocontext workflow[38] and semantic classes for somata, processes and background. We have trained a single Autocontext project with sparse annotations on five regions (CA1, granular layer of cerebellum, molecular layer of cerebellum, hypothalamus, thalamus), with four label classes in the first round of Autocontext: soma, background, and two classes for processes. In the second Autocontext round, we used three different labels, for soma, background, and process. Probability images were generated for all 16 image volumes with ilastik in headless mode using the trained Autocontext project.

We have relied on the feature extraction pipeline of the ilastik Object Classification workflow to extract morphological features. Before processing in ilastik, we have rescaled the probability images to an isotropic resolution of 0.65 µm. Individual somata were extracted by first binarizing the probability maps with a threshold of 0.5 and then performing connected components analysis. We quantified ellipticity by comparing the largest with the smallest eigenvalue of the principal component analysis of the object voxels.

Histological sample preparation. Samples of atherosclerotic human carotid and human keloid (courtesy of R. Cicchi, National Institute of Optics, Italy) were fixed with PFA, cut into 5 µm slices with a microtome, stained with standard hematoxylin–eosin, and mounted in glycerol.

Yeast cultures. The strains used in this study were wild-type *Saccharomyces cerevisiae* (Sigma Aldrich) and *Schizosaccharomyces pombe* (courtesy of I. Tolić, Ruđer Bošković Institute, Croatia), which express GFP-tubulin under the nmt promoter. The yeasts were grown in a standard liquid yeast culture medium (Yeast Peptone D-Glucose) and imaged at 37 °C using a warmed plate. To enhance the expression of GFP, 2 µM thiamine was added to the growing medium of *Schizosaccharomyces pombe*.

***Caenorhabditis elegans* motion assay.** Wild-type *C. elegans* (*C. elegans* Behavior Kit, Bio-Rad Laboratories) was grown according to the protocol recommended by the supplier. To perform the motion assay, a few *C. elegans* worms were transferred with a spatula onto a fresh agar plate and placed under the microscope. Custom software written in LabVIEW 2012 (available from https://github.com/ludovicosilvestri/RAPID_CLSM) was used to keep the worm in the camera field of view. The same software also recorded the XY positions of the stage and worm in the field of view, to provide the absolute XY position of the worm. The Z position was tracked using the position of the Z stage, which was continuously corrected by the RAPID module.

Bright-field and epi-fluorescence microscopy. An Eclipse TE300 inverted microscope (Nikon) equipped with an XYZ stage (L-STEP 13, LANG) was integrated with RAPID for the bright-field and epi-fluorescence experiments. In the bright-field modality, a mercury lamp coupled with a red bandpass filter (630/10, Thorlabs) was used to illuminate the sample. In the epi-fluorescence modality, light from a blue LED (M470L3, Thorlabs) was bandpass-filtered (469/35, Semrock) to avoid contamination in the fluorescence channel and then reflected to a long-pass dichroic mirror (496 nm edge, Semrock) to illuminate the sample. Light emitted from the sample and transmitted by the dichroic mirror was further bandpass-filtered (520/35, Semrock) to isolate the fluorescence contribution. Images were collected using an sCMOS camera (Orca Flash 2.0, Hamamatsu). Defocus was corrected by moving the objective either with a piezo scanner (PIFOC P-721.LLQ, Physik Instrumente, for the yeast cultures) or with the Z axis of the sample translation stage (for the *C. elegans* tracking). The imaging parameters for the different experiments are summarized in Supplementary Table 2.

Reporting Summary. Further information on research design is available in the Nature Research Reporting Summary linked to this article.

Data availability

The datasets acquired for this study are available at https://doi.org/10.25493/AV5J-M46.

Code availability

RAPID stand-alone code is publicly available at https://github.com/lens-biophotonics/RAPID-AF. Code used to control RAPID-enabled LSM is publicly available at https://github.com/ludovicosilvestri/RAPID_CLSM. ZetaStitcher and ilastik are available at https://github.com/lens-biophotonics/ZetaStitcher and https://www.ilastik.org, respectively. BCFind software is available at https://github.com/lens-biophotonics/BCFind2.1.

References

25. Guenthner, C. J., Miyamichi, K., Yang, H. H., Heller, H. C. & Luo, L. Permanent genetic access to transiently active neurons via TRAP: targeted recombination in active populations. *Neuron* **78**, 773–784 (2013).
26. Chung, K. et al. Structural and molecular interrogation of intact biological systems. *Nature* **497**, 332–337 (2013).
27. Costantini, I. et al. A versatile clearing agent for multi-modal brain imaging. *Sci. Rep.* **5**, 9808 (2015).
28. di Giovanna, A. P. et al. Whole-brain vasculature reconstruction at the single capillary level. *Sci. Rep.* **8**, 12573 (2018).
29. Pan, C. et al. Shrinkage-mediated imaging of entire organs and organisms using uDISCO. *Nat. Methods* **13**, 859–867 (2016).
30. Jing, D. et al. Tissue clearing of both hard and soft tissue organs with the PEGASOS method. *Cell Res.* **28**, 803–818 (2018).
31. Müllenbroich, M. C. et al. Comprehensive optical and data management infrastructure for high-throughput light-sheet microscopy of whole mouse brains. *Neurophotonics* **2**, 041404 (2015).
32. Preibisch, S., Saalfeld, S. & Tomancak, P. Globally optimal stitching of tiled 3D microscopic image acquisitions. *Bioinformatics* **25**, 1463–1465 (2009).
33. Frasconi, P. et al. Large-scale automated identification of mouse brain cells in confocal light sheet microscopy images. *Bioinformatics* **30**, i587–93 (2014).
34. Galil, Z. Efficient algorithms for finding maximum matching in graphs. *ACM Comput. Surv.* **18**, 23–38 (1986).
35. Avants, B. B. et al. A reproducible evaluation of ANTs similarity metric performance in brain image registration. *Neuroimage* **54**, 2033–2044 (2011).
36. Jafari-Mamaghani, M., Andersson, M. & Krieger, P. Spatial point pattern analysis of neurons using Ripley's K-function in 3D. *Front. Neuroinform.* **4**, 9 (2010).
37. Berg, S. et al. ilastik: interactive machine learning for (bio)image analysis. *Nat. Methods* **16**, 1226–1232 (2019).

38. Kreshuk, A. & Zhang, C. Machine learning: advanced image segmentation using ilastik. *Methods Mol. Biol.* **2040**, 449–463 (2019).

Acknowledgements

The authors thank F. Del Gallo from the University of Padova (Italy) for providing mouse brain with labeled microglia, I. Tolić from the Ruđer Bošković Institute (Croatia) for providing the fluorescent *Schizosaccharomyces pombe*, and R. Cicchi from the National Institute of Optics (Italy) for providing the histological slides used in this study. This project received funding from the European Union's Horizon 2020 research and innovation program under grant agreements no. 785907 (Human Brain Project) and 871124 (Laserlab-Europe), and from the H2020 EU program Excellent Science in conjunction with the European Research Council (ERC) under grant agreement ID no. 692943 (BrainBIT). The project has also been supported by the Italian Ministry for Education, University, and Research within the framework of the Flagship Project NanoMAX and of the Advance Lightsheet Microscopy Italian Mode of Euro-Bioimaging ERIC, and by Ente Cassa di Risparmio di Firenze (a private foundation). M.C.M. acknowledges a Marie Skłodowska-Curie fellowship (MSCA-IF-EF-ST grant agreement no. 842893).

Author contributions

L. Silvestri devised RAPID; L. Silvestri, L. Sacconi and F.S.P. designed the experiments; L. Silvestri and M.C.M. implemented RAPID; L. Silvestri and G.M. developed RAPID standalone software; I.C. prepared the yeast and nematode samples; A.P.D.G. and I.C. prepared the cleared mouse brains; L. Silvestri, I.C. and A.P.D.G. performed the experiments; L. Silvestri and M.C.M. analyzed data; L. Silvestri, L.O.T., A. F. and I.C. manually annotated ground-truth data for cell localization; C.C., L.O.T., G.M. and P.F. analyzed whole-brain SST+ datasets, and performed stitching and cell localization; D.K. and A.K. analyzed microglia morphology data; and L. Silvestri and M.C.M. wrote the paper with contributions from all of the authors.

Competing interests

L. Silvestri, M.C.M., L. Sacconi and F.S.P. are inventors of patent IT201600132604A1, which is related to RAPID. All other authors have no competing interests.

Additional information

Extended data are available for this paper at https://doi.org/10.1038/s41592-021-01208-1.

Supplementary information The online version contains supplementary material available at https://doi.org/10.1038/s41592-021-01208-1.

Correspondence and requests for materials should be addressed to L.S.

Peer review information *Nature Methods* thanks Adam Glaser and the other, anonymous, reviewer(s) for their contribution to the peer review of this work. Rita Strack was the primary editor on this article and managed its editorial process and peer review in collaboration with the rest of the editorial team.

Reprints and permissions information is available at www.nature.com/reprints.

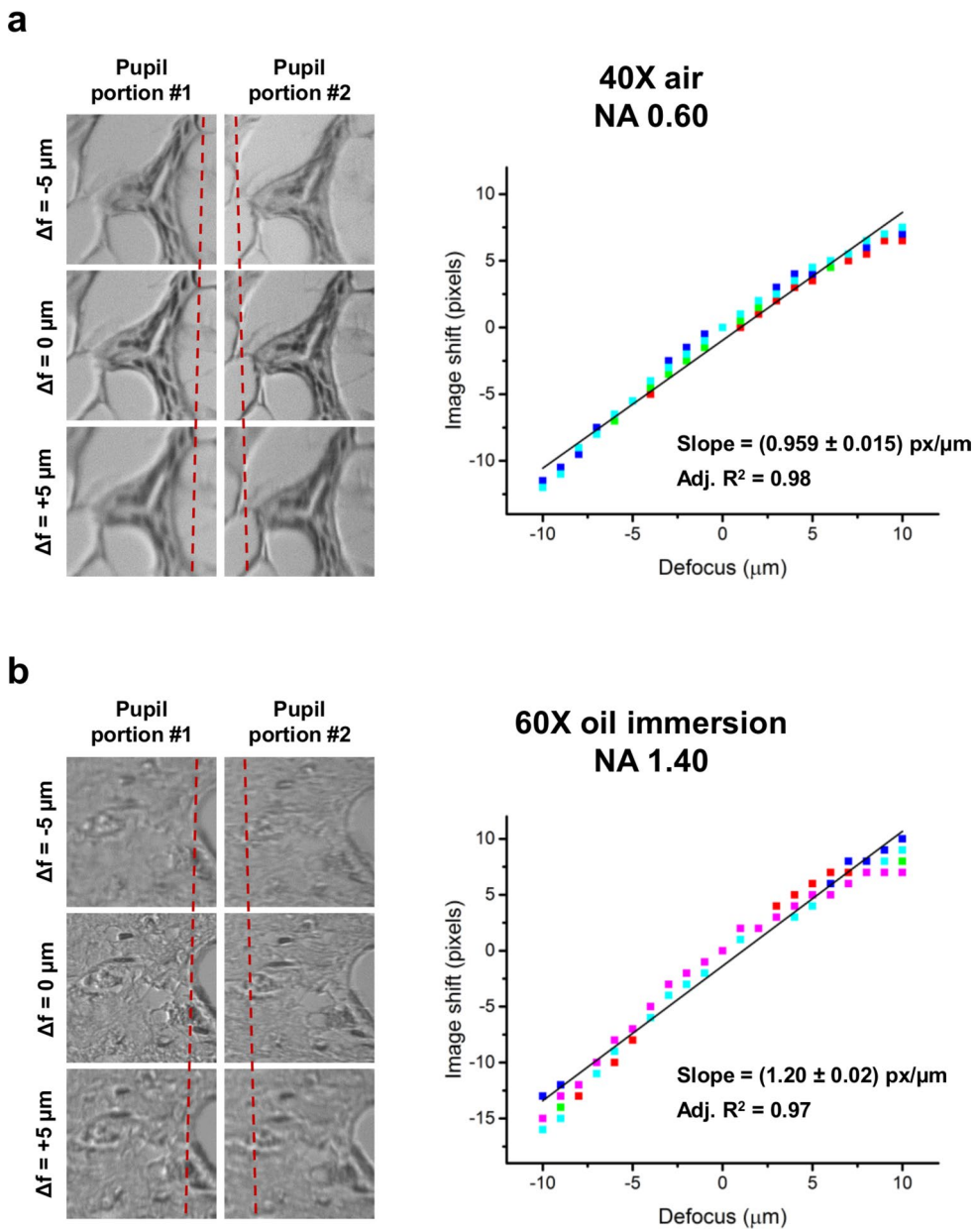

Extended Data Fig. 1 | Lateral shift of pupil-split images in brightfield microscopy. Mutual lateral displacement of the two pupil-split images in brightfield illumination settings, for two different objectives (**a** and **b**). For these measurements, histological keloid samples stained with hematoxylin and eosin were used. Left panels show examples of the image shifts, with a dashed red line to help the reader visualizing the small lateral displacements. Right panels show image shifts determined by automatic image analysis as a function of defocus; different colors identify distinct defocus stacks. A linear fit with the measured slope and a measure of fit goodness (the adjusted R^2 score) is also shown.

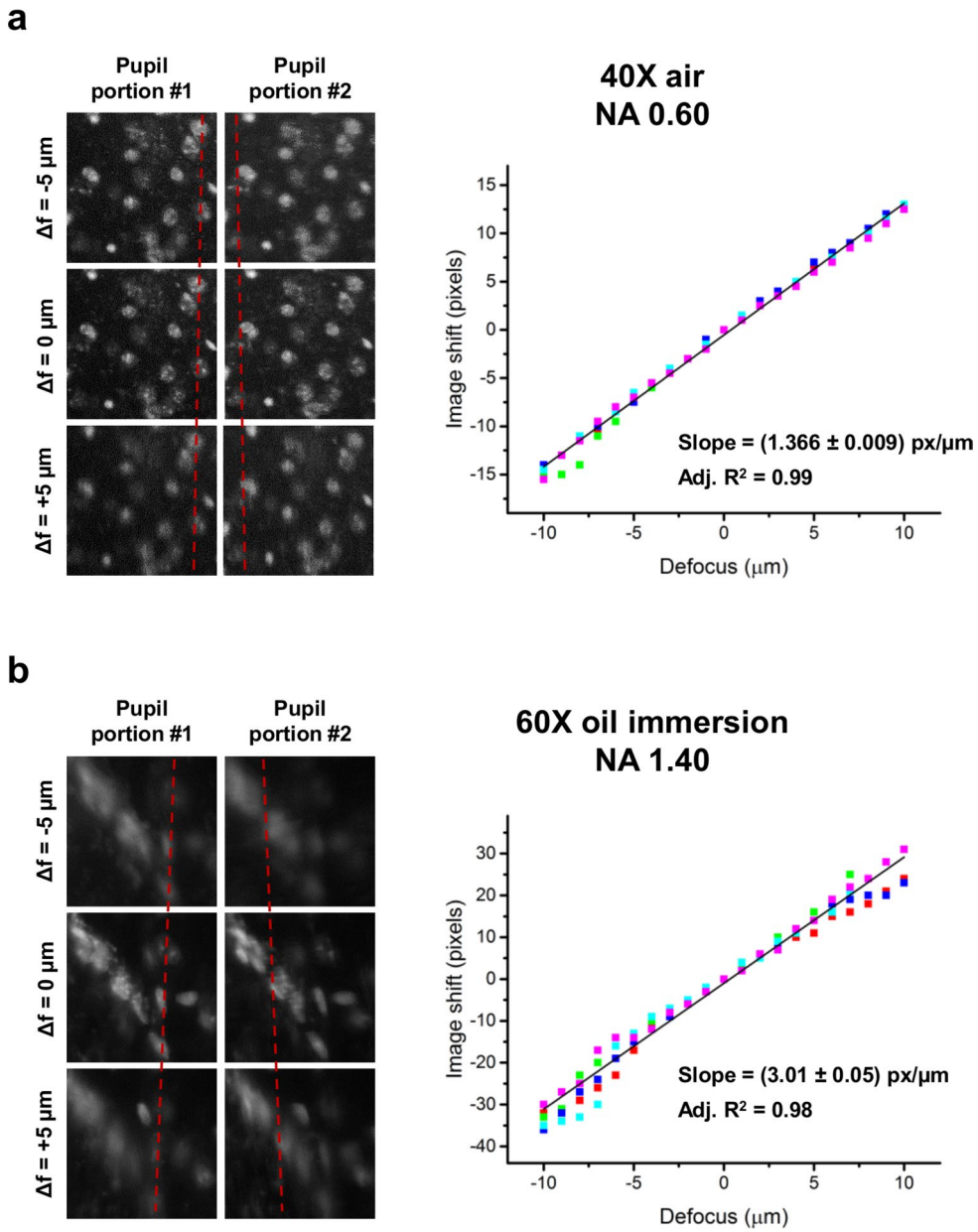

Extended Data Fig. 2 | Lateral shift of pupil-split images in epifluorescence microscopy. Mutual lateral displacement of the two pupil-split images in epifluorescence illumination settings, for two different objectives (**a** and **b**). For these measurements, mouse brain slices stained with SYTOX Green Nucleic Acid Stain (ThermoFisher) were used. Left panels show examples of the image shifts, with a dashed red line to help the reader visualize the small lateral displacements. Right panels show image shifts determined by automatic image analysis as a function of defocus; different colors identify distinct defocus stacks. A linear fit with the measured slope and a measure of fit goodness (the adjusted R^2 score) is also shown.

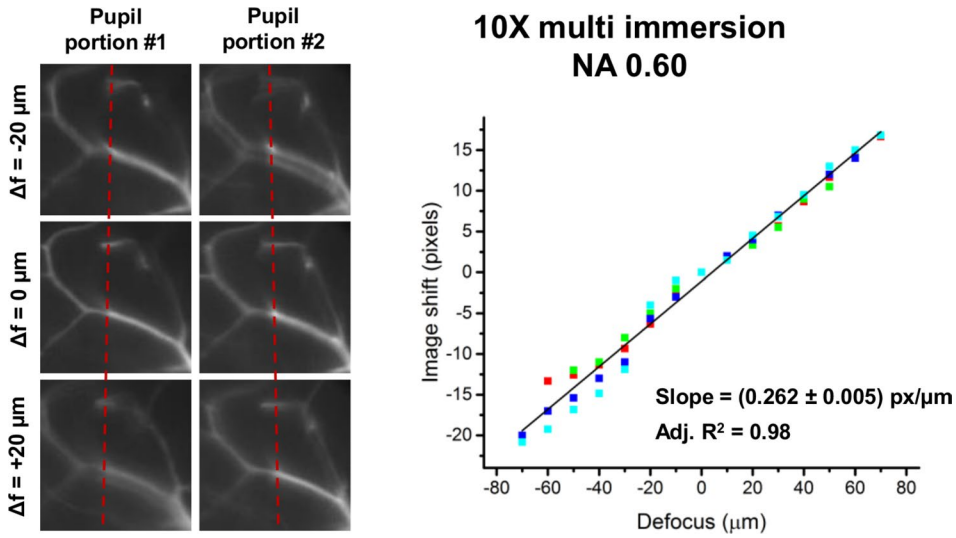

Extended Data Fig. 3 | Lateral shift of pupil-split images in light-sheet fluorescence microscopy. Mutual lateral displacement of the two pupil-split images in light-sheet illumination settings. For these measurements, cleared mouse brains with vasculature fluorescent filling were used. Left panel shows examples of the image shifts, with a dashed red line to help the reader visualize the small lateral displacements. Right panel shows image shifts determined by automatic image analysis as a function of defocus; different colors identify distinct defocus stacks. A linear fit with the measured slope and a measure of fit goodness (the adjusted R^2 score) is also shown. Note that quite good linearity is observed over a range of 140 µm, about 70 times larger than the objective depth of focus (≈ 2 µm).

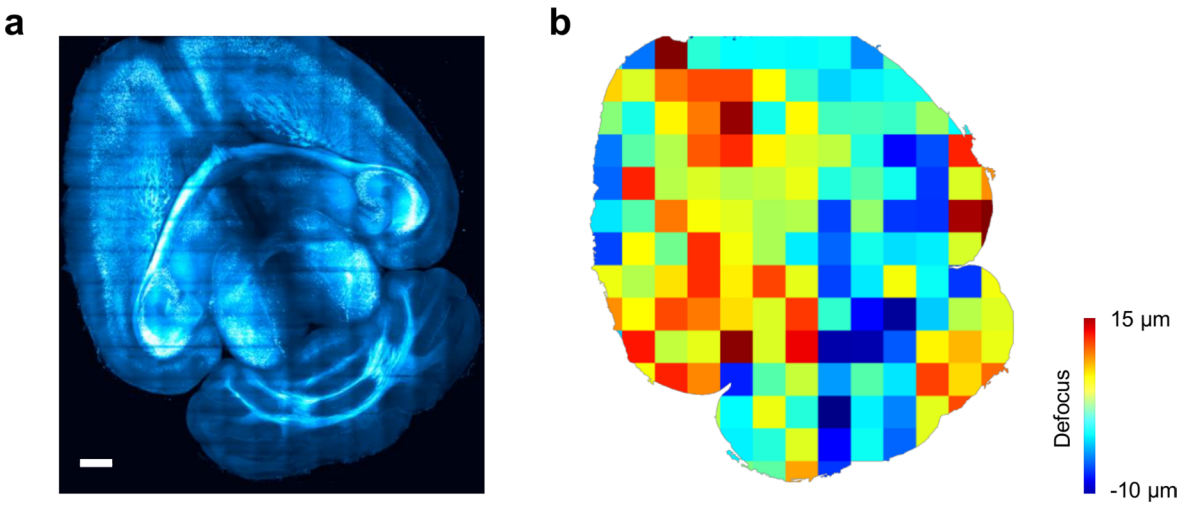

Extended Data Fig. 4 | Defocus variability in clarified mouse brains. a, Virtual slab (500 µm thick) from the brain of a thy1-GFP-M mouse. **b**, Average defocus for each tile, denoting a clear focal difference between the two light sheets used to illuminate the two halves of the brain, as well as variable defocusing across tiles. Scale bar, 1 mm.

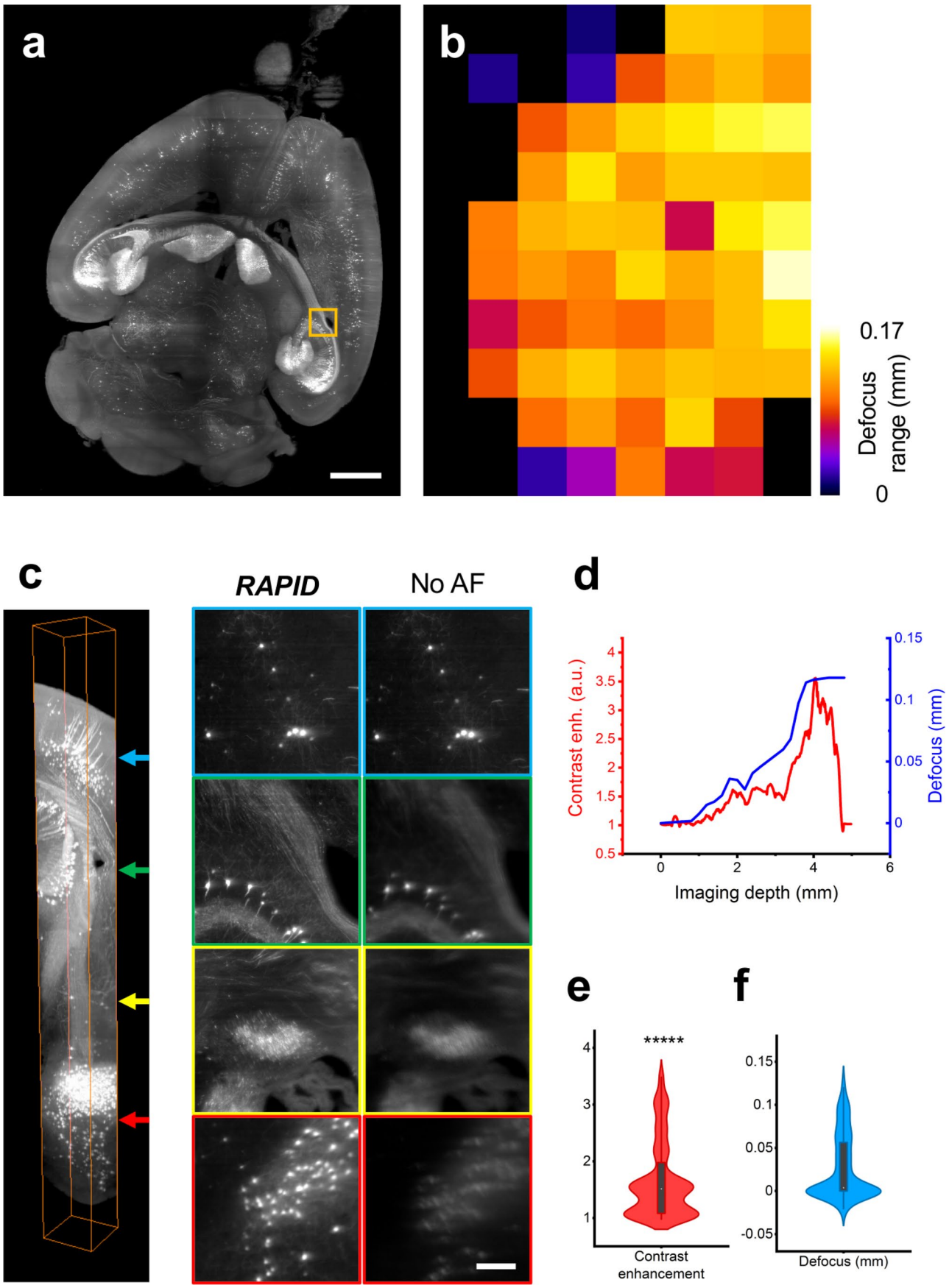

Extended Data Fig. 5 | See next page for caption.

Extended Data Fig. 5 | RAPID-enabled LSM on uDISCO cleared mouse brain. a, Virtual slab extracted from the whole brain of a Thy1-GFP-M mouse cleared with uDISCO. For imaging, the sample was immersed in BABB-D10 (refractive index n = 1.56). The imaging chamber surrounding the sample cuvette was filled with TDE (n = 1.52). **b**, defocus range (that is absolute value of maximum variation in defocus) in the different image stacks collected to reconstruct the entire volume. **c**, 3D rendering of a portion of stack, highlighted with the orange square in (**a**), together with example images taken at different depths either with or without RAPID focus correction. **d**, Contrast enhancement obtained using RAPID and defocus as a function of depth for the image stack shown in **c**, **e**, violin plot of the contrast enhancement shown in (**d**). This distribution is significantly higher than 1, with p-value $< 10^{-5}$ (one-sample Student t-test, n = 2490 images). **f**, violin plot of the defocus across the entire tomography volume (n = 1040 defocus positions). Scale bars: 1 mm **a**, and 100 μm **c**,. In the violin plots shown in **e**,**f**, data are also presented as box plots with minima at 5 percentile, maxima at 95 percentile, center at 50 percentile, and bounds of box at 25 and 75 percentile, respectively.

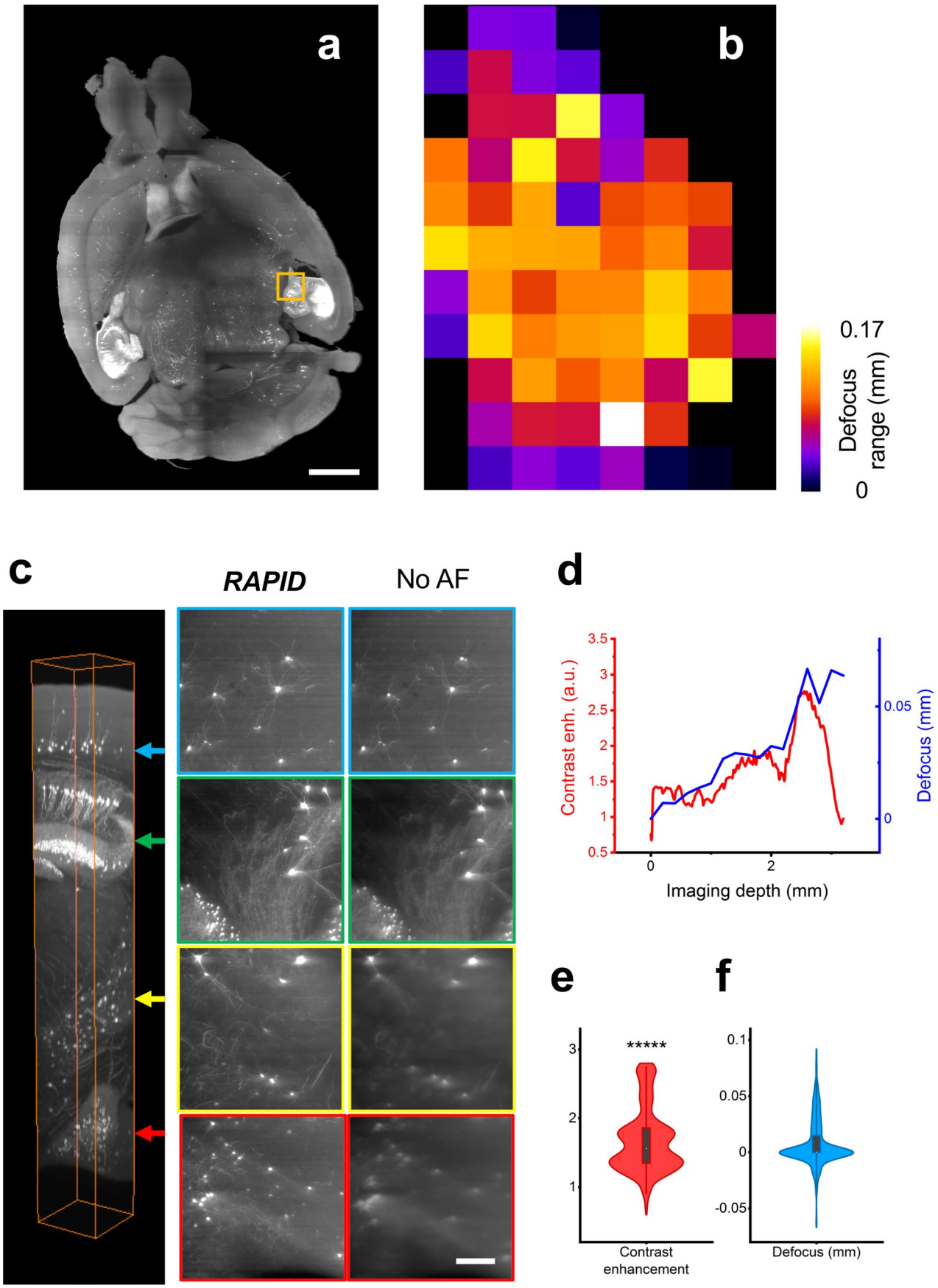

Extended Data Fig. 6 | See next page for caption.

Extended Data Fig. 6 | RAPID-enabled LSM on PEGASOS cleared mouse brain. a, Virtual slab extracted from the whole brain of a Thy1-GFP-M mouse cleared with PEGASOS. For imaging, the sample was immersed in BB-PEG (refractive index n = 1.543). The imaging chamber surrounding the sample cuvette was filled with TDE (n = 1.52). **b**, defocus range (that is absolute value of maximum variation in defocus) in the different image stacks collected to reconstruct the entire volume. **c**, 3D rendering of a portion of stack, highlighted with the orange square in (**a**), together with example images taken at different depths either with or without RAPID focus correction. **d**, Contrast enhancement obtained using RAPID and defocus as a function of depth for the image stack shown in (c) **e**, violin plot of the contrast enhancement shown in **d**, This distribution is significantly higher than 1, with p-value $< 10^{-5}$ (one-sample Student t-test, n = 1600 images). **f** violin plot of the defocus across the entire tomography volume (n = 1248 defocus positions). Scale bars: 1 mm (**a**), and 100 μm **c**, In the violin plots shown in (**e**,**f**), data are also presented as box plots with minima at 5 percentile, maxima at 95 percentile, center at 50 percentile, and bounds of box at 25 and 75 percentile, respectively.

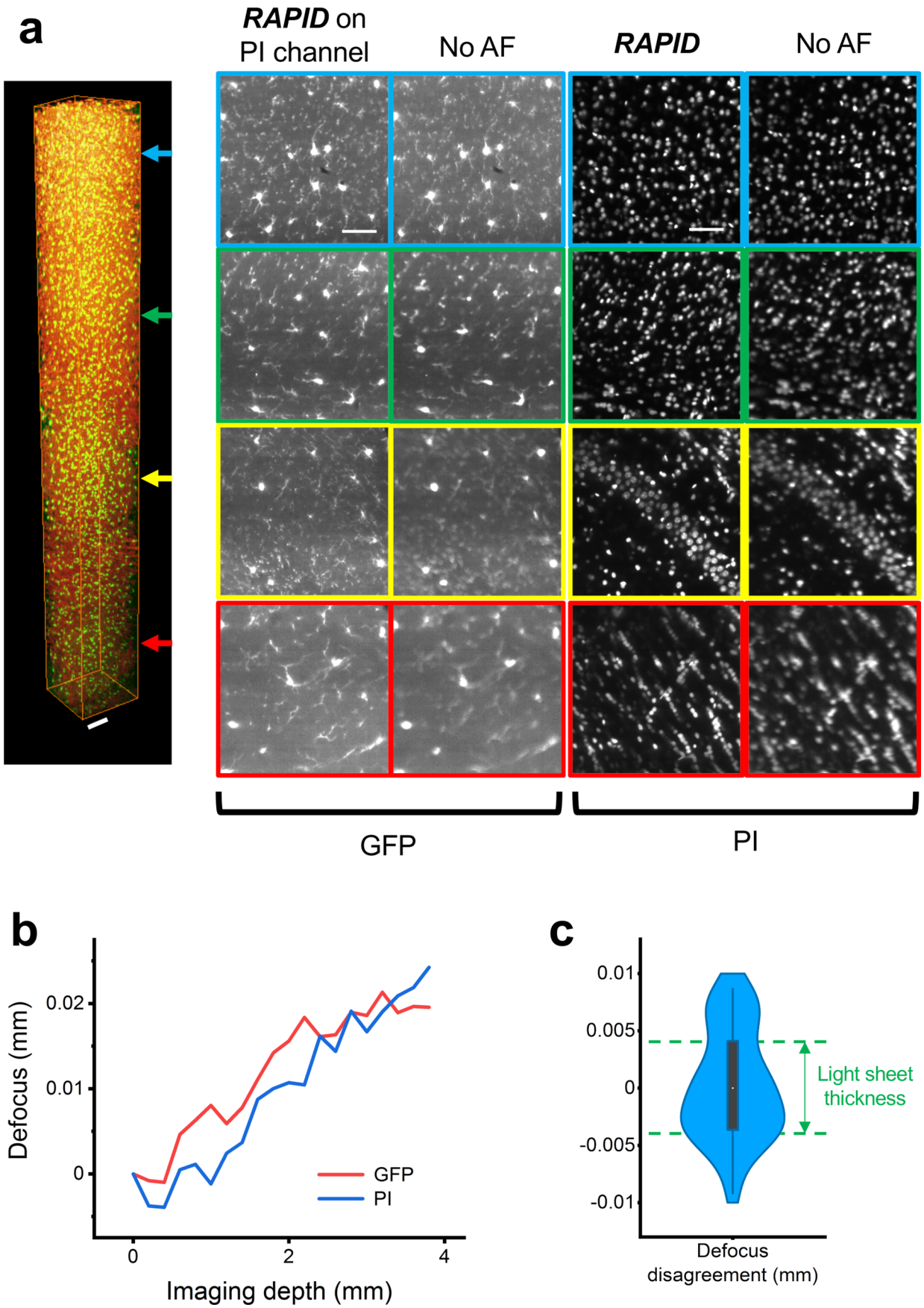

Extended Data Fig. 7 | See next page for caption.

Extended Data Fig. 7 | Multi-color RAPID autofocusing. a, On the left, 3D rendering of a stack imaged in two channels (GFP and PI, with RAPID autofocusing operating on PI channel). On the right, example images of both channels taken at different depths, either with or without RAPID focus correction. Scale bars: 200 μm (rendering), 100 μm (insets). **b**, RAPID defocus in the stack, computed using the GFP or PI channel, respectively. **c**, Violin plot of the discrepancy between defocus computed using the two channels (n = 40 defocus points). In the same panel, data are also presented as box plots with minima at 5 percentile, maxima at 95 percentile, center at 50 percentile, and bounds of box at 25 and 75 percentile, respectively. The same graph reports also the thickness of the light sheet.

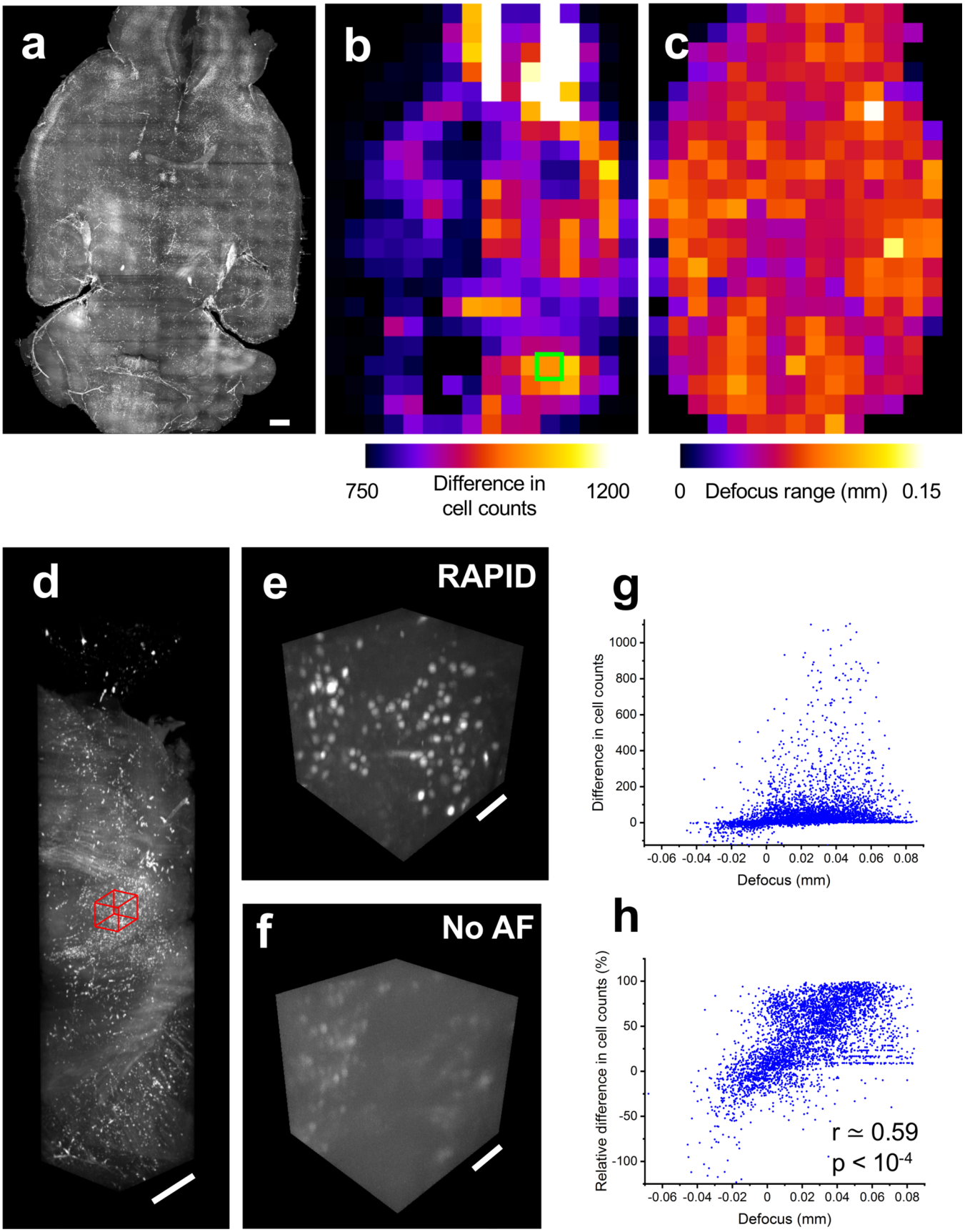

Extended Data Fig. 8 | See next page for caption.

Extended Data Fig. 8 | RAPID autofocusing allows robust cell localization. a,Virtual slab extracted from the whole brain of a FosTRAP mouse. **b**, Difference in cell counts between stacks imaged with RAPID autofocus and the same imaged without defocus correction. **c**, defocus range in the different image stacks collected to reconstruct the entire volume. **d**, 3D rendering of a stack, highlighted with the green square in (**b**). **e**, high-resolution 3D rendering of the portion of stack highlighted with the red parallelepiped in (**d**), imaged with RAPID autofocus. (f) the same volume shown in **e**, imaged without defocus correction. **g**, difference in cell counts (RAPID – No AF) versus defocus, calculated for subvolumes of $1\times1\times0.4\,mm^3$. **h**, relative difference in cell counts (RAPID – No AF) versus defocus, calculated on the same subvolumes. The graph reports also Pearson's correlation coefficient r between the two variables and the probability p that the observed correlation is due to chance. Scale bars: 1 mm (**a**, **b**, **c**, **d**) and 100 μm (**e**, **f**).

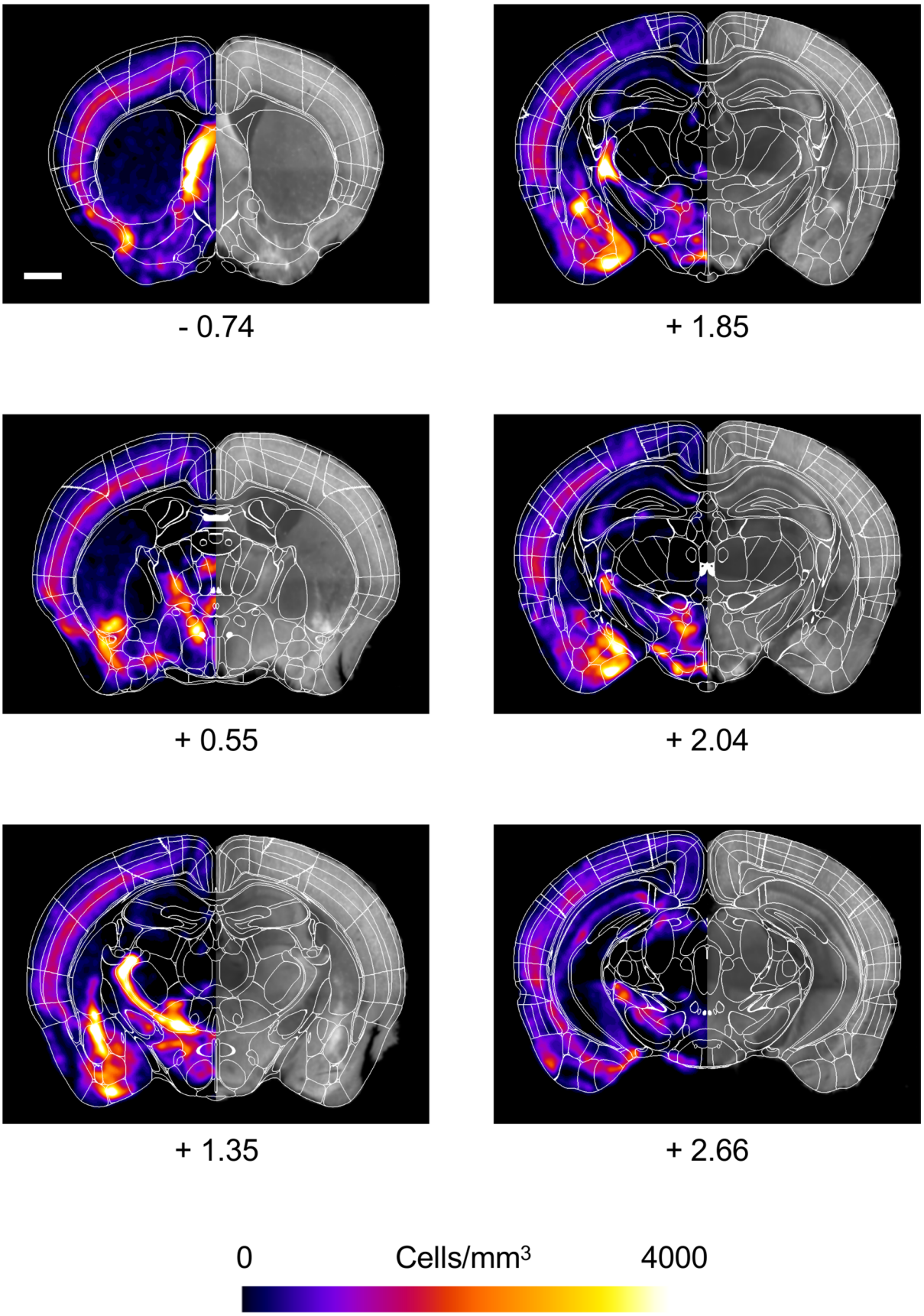

Extended Data Fig. 9 | Spatial distribution of SST+ cells. Coronal slices taken at different anterior/posterior positions, showing density heatmap (left half), original grayscale image (right half, gamma corrected to reduce dynamic range). Contours from Allen brain Common Coordinate Framework (CCF v3) are superimposed. Consistently with previous reports[18], SST cortical neurons are mainly located in layer 4. Numbers represents A/P bregma. Scale bar, 1 mm.

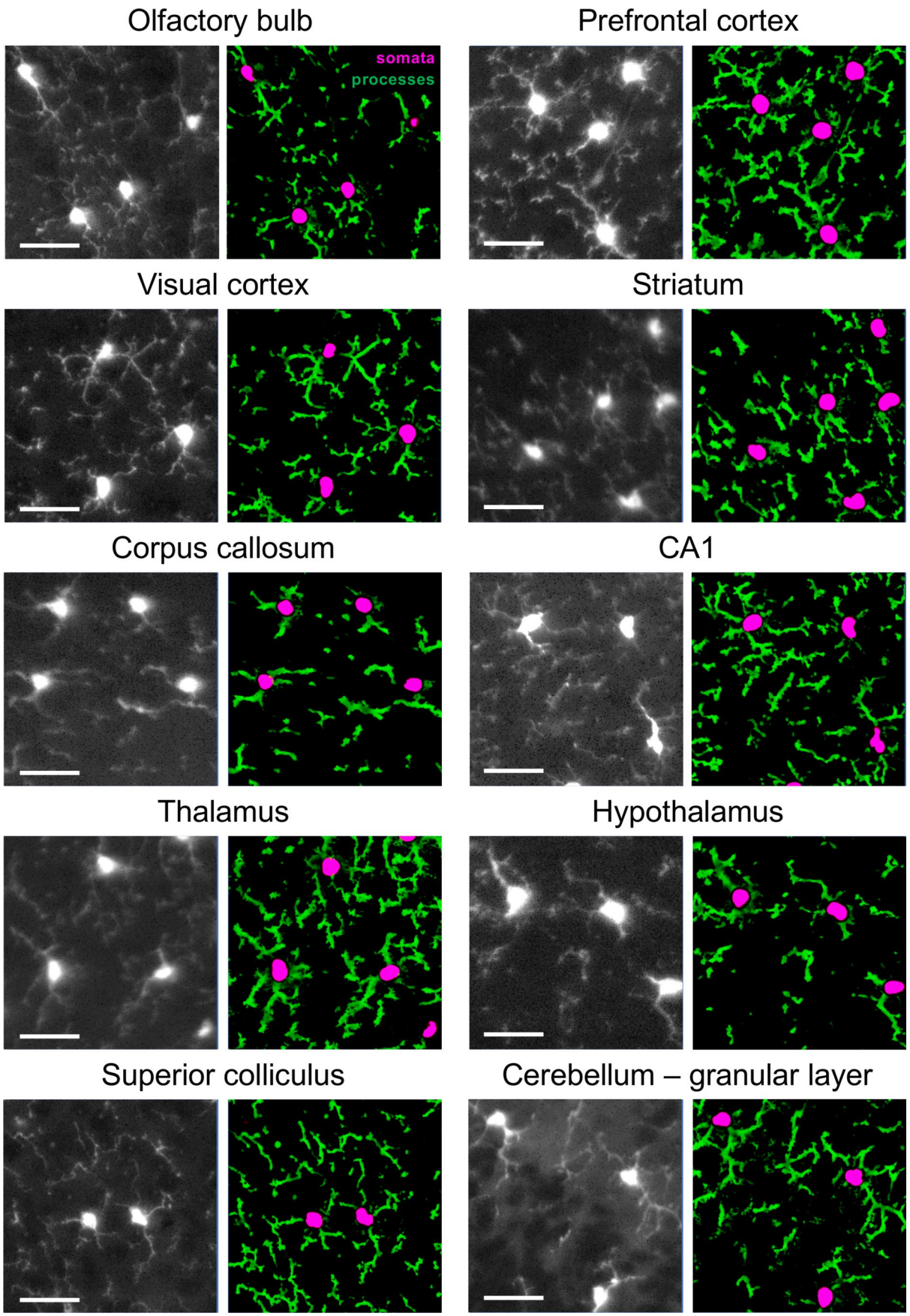

Extended Data Fig. 10 | Microglia segmentation across multiple brain areas. Representative images of microglia cells from different mouse brain areas, together with the results of the Ilastik segmentation. Somata are depicted in magenta, processes in green. Scale bar, 50 μm; scale is the same for all images.

nature research

Corresponding author(s): Ludovico Silvestri

Last updated by author(s): May 30, 2021

Reporting Summary

Nature Research wishes to improve the reproducibility of the work that we publish. This form provides structure for consistency and transparency in reporting. For further information on Nature Research policies, see our Editorial Policies and the Editorial Policy Checklist.

Statistics

For all statistical analyses, confirm that the following items are present in the figure legend, table legend, main text, or Methods section.

n/a	Confirmed	
☐	☒	The exact sample size (*n*) for each experimental group/condition, given as a discrete number and unit of measurement
☒	☐	A statement on whether measurements were taken from distinct samples or whether the same sample was measured repeatedly
☐	☒	The statistical test(s) used AND whether they are one- or two-sided *Only common tests should be described solely by name; describe more complex techniques in the Methods section.*
☒	☐	A description of all covariates tested
☒	☐	A description of any assumptions or corrections, such as tests of normality and adjustment for multiple comparisons
☐	☒	A full description of the statistical parameters including central tendency (e.g. means) or other basic estimates (e.g. regression coefficient) AND variation (e.g. standard deviation) or associated estimates of uncertainty (e.g. confidence intervals)
☐	☒	For null hypothesis testing, the test statistic (e.g. *F*, *t*, *r*) with confidence intervals, effect sizes, degrees of freedom and *P* value noted *Give P values as exact values whenever suitable.*
☒	☐	For Bayesian analysis, information on the choice of priors and Markov chain Monte Carlo settings
☒	☐	For hierarchical and complex designs, identification of the appropriate level for tests and full reporting of outcomes
☒	☐	Estimates of effect sizes (e.g. Cohen's *d*, Pearson's *r*), indicating how they were calculated

Our web collection on statistics for biologists contains articles on many of the points above.

Software and code

Policy information about availability of computer code

Data collection	Code for microscope operation and stand-alone code for RAPID are available at https://github.com/ludovicosilvestri/RAPID_CLSM and https://github.com/lens-biophotonics/RAPID-AF, respectively
Data analysis	ZetaStitcher is available at https://github.com/lens-biophotonics/ZetaStitcher, Ilastik at https://www.ilastik.org, BCFind (code used for neuronal soma localization) at https://github.com/lens-biophotonics/BCFind2.1

For manuscripts utilizing custom algorithms or software that are central to the research but not yet described in published literature, software must be made available to editors and reviewers. We strongly encourage code deposition in a community repository (e.g. GitHub). See the Nature Research guidelines for submitting code & software for further information.

Data

Policy information about availability of data

All manuscripts must include a data availability statement. This statement should provide the following information, where applicable:

- Accession codes, unique identifiers, or web links for publicly available datasets
- A list of figures that have associated raw data
- A description of any restrictions on data availability

All data are available on the eBRAINS public repository, at the link specified in the Data Availability Statement

Field-specific reporting

Please select the one below that is the best fit for your research. If you are not sure, read the appropriate sections before making your selection.

☒ Life sciences ☐ Behavioural & social sciences ☐ Ecological, evolutionary & environmental sciences

For a reference copy of the document with all sections, see nature.com/documents/nr-reporting-summary-flat.pdf

Life sciences study design

All studies must disclose on these points even when the disclosure is negative.

Sample size	Sample size for contrast enhancement analysis (e.g. Ext. Data Fig. 5e) was justified a posteriori since differences were statistically significant. Sample size for distribution or shape analysis (Figs. 2h-j, 3d-f) or for defocus statistics (e.g. Ext. Data Fig. 5f) consisted of all cells or of all defocus positions registered. In this case the entire sample was used. Sample size of training and validation data for image processing (e.g. Supp. Fig. 10) was limited by the manpower required to perform manual labeling, and was justified a posteriori by assessign the quality of segmentation or localization.
Data exclusions	No data were excluded.
Replication	We checked autofocus performances on many different samples (cleared mouse brains), with different methodologies for sample preparation (CLARITY, uDISCO, PEGASOS), and different microscopy techniques (light-sheet microscopy, brightfield microscopy, epifluorescence microscopy). All replication attempts were successful.
Randomization	Image stacks used to quantify accuracy of automated cell detection or microglia segmentation were randomly selected from sample volume.
Blinding	Blinding is not relevant to our study since we do not aim at evaluating differences between groups but at validating the performance of a new microscopy method. Indeed, we do not have different experimental sample groups. We compared different techniques (imaging with and without autofocus) on the same samples.

Reporting for specific materials, systems and methods

We require information from authors about some types of materials, experimental systems and methods used in many studies. Here, indicate whether each material, system or method listed is relevant to your study. If you are not sure if a list item applies to your research, read the appropriate section before selecting a response.

Materials & experimental systems

n/a	Involved in the study
☒	☐ Antibodies
☐	☒ Eukaryotic cell lines
☒	☐ Palaeontology and archaeology
☐	☒ Animals and other organisms
☒	☐ Human research participants
☒	☐ Clinical data
☒	☐ Dual use research of concern

Methods

n/a	Involved in the study
☒	☐ ChIP-seq
☒	☐ Flow cytometry
☒	☐ MRI-based neuroimaging

Eukaryotic cell lines

Policy information about cell lines

Cell line source(s)	Yeast cell lines used in this study were: wild-type Saccharomyces cerevisiae (Sigma-Aldrich, St. Louis, MO) and Schizosaccharomyces pombe (that express GFP-tubulin under the nmt promoter, courtesy of Prof. Tolić, Ruđer Bošković Institute, Croatia).
Authentication	Cell lines were not authenticated because this step was not essential to support the conclusions of the study.
Mycoplasma contamination	Cell lines were not tested for mycoplasma contamination because this step was not essential to support the conclusions of the study.
Commonly misidentified lines (See ICLAC register)	No commonly misidientified lines were used.

Animals and other organisms

Policy information about studies involving animals; ARRIVE guidelines recommended for reporting animal research

Laboratory animals	Mice (mus musculus), male, killed at post-natal day 56. Strains used: thy1-GFP-M, B6N.Cg-Ssttm2.1(cre)Zjh/J × B6.Cg-Gt(ROSA)26Sortm9(CAG-tdTomato)Hze/J, B6.129(Cg)-Fostm1.1(cre/ERT2)Luo/J × B6.Cg-Gt(ROSA)26Sortm9(CAG-tdTomato)Hze/J, B6.129P2(Cg)-Cx3cr1tm1Litt/J, C57 wild-type.
Wild animals	This study did not involve wild animals
Field-collected samples	This study did not involve sample collection from the field
Ethics oversight	All protocols involving animals were approved by the Italian Ministry of Health (authorization n. 790/2016-PR).

Note that full information on the approval of the study protocol must also be provided in the manuscript.